이학석사 학위논문

Direct Visualization of Plasmonic Hotspots of Silver Nanowire Dimers using SERS

표면증강라만산란을 응용한 은 나노선 이합체의 플라즈몬 핫스팟에 대한 직접적인 가시화

2018년 2월

서울대학교 대학원

화학부 물리화학전공

박 상 민

M. S. Dissertation

Direct Visualization of Plasmonic Hotspots of Silver Nanowire Dimers using SERS

Supervisor : Professor Zee Hwan Kim

February 2018

By Sang-Min Park

Department of Chemistry

The Graduate School

Seoul National University

Abstract

Direct Visualization of Plasmonic Hotspots of Silver Nanowire Dimers using SERS

Sang-Min Park
Physical Chemistry Major
Department of Chemistry
The Graduate School
Seoul National University

Visualization of surface plasmon polaritons (SPP) is essential for characterization of plasmonic waveguides which are building blocks for photonic circuits with subwavelength scale. Currently, well-established techniques such as fluorescence- or tip-based microscopy usually improper for being applied to narrow-gap plasmonic structures. In this case, surface-enhanced Raman scattering (SERS) microscopy can be an alternative tool for visualizing highly localized electric field of gap plasmon waveguides.

In this work, we report on SERS imaging of chemically synthesized silver nanowire (AgNW) dimers, which shows spatial modulation of intensity patterns along NW-axis. We interpret that such unusual SERS patterns arise from mode beating between two distinct SPP eigenmodes of NW-dimers, generating oscillating intensity distributions. Also, we discuss the validity of the concept that SERS intensity at far-field region directly represents the

intensity of local electric field generated from plasmon excitation process, contrary to usual nanoparticle dimers cases.

Keyword : Surface-enhanced Raman scattering, plasmonic waveguide, silver nanowire, surface plasmon polariton, gap plasmon
Student Number : 2016-20342

Table of Contents

Table of Figures

1. Introduction

Visualization techniques for near-field characters of plasmonic nanostructure combined with spectroscopic information are becoming more important for designing optical devices with spatial dimension of subwavelength scale. Here, we suggest that wide-field surface-enhanced Raman scattering (SERS) imaging is a prospective candidate for visualizing highly confined surface plasmon polaritons at narrow gap of plasmonic waveguides. To understand basic idea of this wide-field SERS imaging technique, we briefly look over basic concepts about plasmon (1.1), especially surface plasmon polaritons (SPPs) at metallic waveguides (1.2) and pre-existing techniques related to visualization of SPPs (1.2.3). Then, we will explore the basic principles of surface-enhanced Raman scattering.

1.1. Plasmon

Plasmon is collective oscillation of free electrons in metal. Two distinct types of surface plasmons are known to exist depending on the geometry of the metal. At finite cavity with size of subwavelength scale, plasmon acts as 'localized surface plasmon (LSP)'. However, at a flat metal-dielectric interface, plasmon propagates along the interface as 'surface plasmon polariton (SPP)'.

1.1.1. Localized Surface Plasmon

A localized surface plasmon is caused by the confinement of a surface plasmon in nanoparticles of size comparable to or smaller than the wavelength of light in vacuum used to launch the plasmon. (see figure 1)

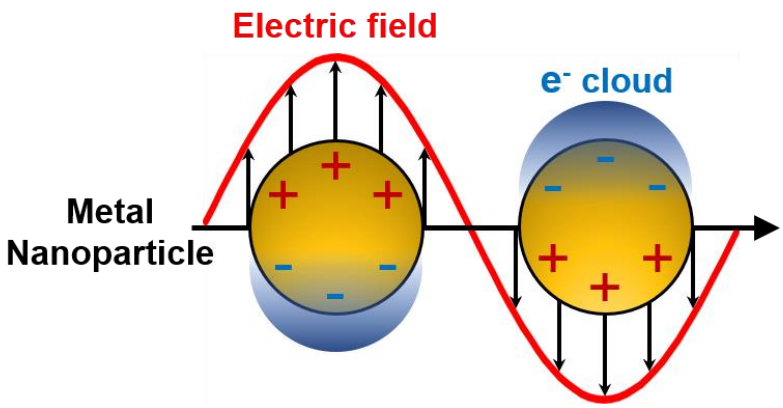

Figure 1. Schematic illustration for localized surface plasmon resonance at metal nanoparticle.

1.1.2. Surface Plasmon Polariton

Surface plasmons are collective oscillations of free electrons that exist between flat metal–dielectric interface. When surface plasmons are coupled to photons, they can create electromagnetic waves which propagate along interface known as surface plasmon–polariton (SPP). The schematic illustration for electromagnetic field

of SPPs is depicted in Figure 2. The electric field is highly confined to the vicinity of the metal-dielectric interface and decays exponentially along the direction perpendicular to metal surface.

Thanks to their sub-wavelength and local field enhancement effects, SPPs can be applied in diverse areas, such as the near-field microscopy[1-3], bio- and chemical sensors[4][5], enhanced Raman[5-7], nonlinear optics[8] and nanophotonics[9-11].

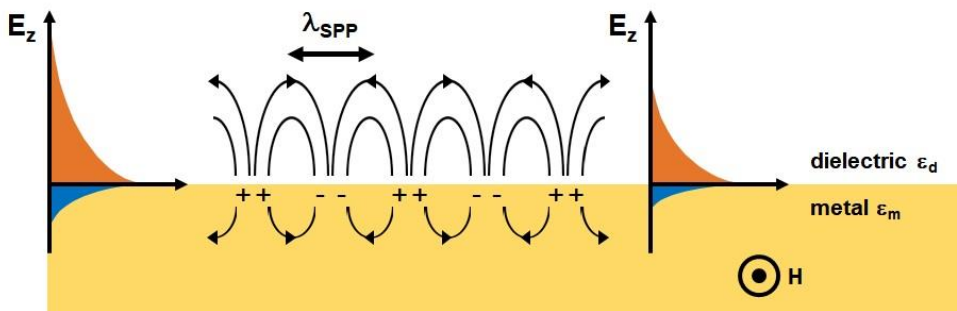

Figure 2. A surface plasmon polariton is a charge density wave which travels through the metal-dielectric interface.

1.2. SPP Propagation in Metal Waveguide

Metal nanowires can support SPPs propagating along longitudinal axis of nanowire while localizing SPPs in the other two perpendicular axes. Those SPPs can be described as sum of eigenmodes determined by NW's perpendicular cross section and its environment.

Each eigenmode in specific NW has distinct propagation characteristics, such as, field confinement, propagation length, surface charge density distribution, and momentum. Those characteristics can be calculated using 2-dimensional numerical Maxwell solver, for instance, finite element method and finite time difference domain method.

Song et al[13]. reported that eigenmode solver based on finite element method can provide effective index of each eigenmode exists in silver nanowire on glass substrate. Moreover, they successfully shown that experimentally measured effective indices, measured from Fourier image of leakage microscopy, match well with those predicted from numerically solved eigenmodes.

1.2.1. Eigenmodes of Waveguide

An eigenmode of the waveguide is a propagating wave of which the transversal cross-sectional shape does not change during propagation. A typical example is shown in figure 2. When we choose the z-direction as the propagation direction, we can write the refractive index profile of waveguide's cross section as below.

$$n = n(x, y) \qquad \text{(Eq. 1)}$$

An eigenmode propagating in the positive z-direction is represented by electric field or magnetic field described below.

$$\boldsymbol{E} = \boldsymbol{e}(x,y)\cdot e^{-i\beta z} \quad \text{(Eq. 2)}$$

$$\boldsymbol{H} = \boldsymbol{h}(x,y)\cdot e^{-i\beta z} \quad \text{(Eq. 3)}$$

In this case, electric field E (or magnetic field H) is described by product of two terms which are electric mode profile $\mathbf{e}(x,y)$ (or magnetic mode profile $\mathbf{h}(x,y)$), and phase term $e^{-i\beta z}$. Consequently, the propagation constant β is used to describe the propagation properties of the eigenmode.

1.2.2. Effective Indices of Eigenmodes

For light in transparent homogeneous dielectric media, the refractive index n can be used to quantify the increase in the wavenumber (phase change per unit length) caused by media. The effective index, n_{eff}, has the homologous meaning for electromagnetic wave propagation in a waveguide with restricted transverse extension: the n_{eff} value of the waveguide is the β value divided by wavenumber (k_0) in vacuum.

$$n_{\text{eff}} = \frac{\beta}{k_0} \quad \text{(Eq. 4)}$$

The mode-dependent and frequency-dependent n_{eff} values can be obtained from numerical Maxwell solver based on finite element method, or finite difference time domain method. The effective index depends on the refractive index profile of the

waveguide's cross-sectional structure. (see figure 3)

Note that the effective refractive index depends not only on the frequency of the electromagnetic wave but also on the eigenmode in which the light propagates.

The effective index is a complex quantity. The real part (n') describes wavenumber (k_z) of electromagnetic wave, and the imaginary part (n") describes propagation loss (L).[14-16]

$$n_{\text{eff}} = n' + in" \quad \text{(Eq. 5)}$$

$$k_z = n' k_0 \quad \text{(Eq. 6)}$$

$$L = \frac{1}{2n" k_0} \quad \text{(Eq. 7)}$$

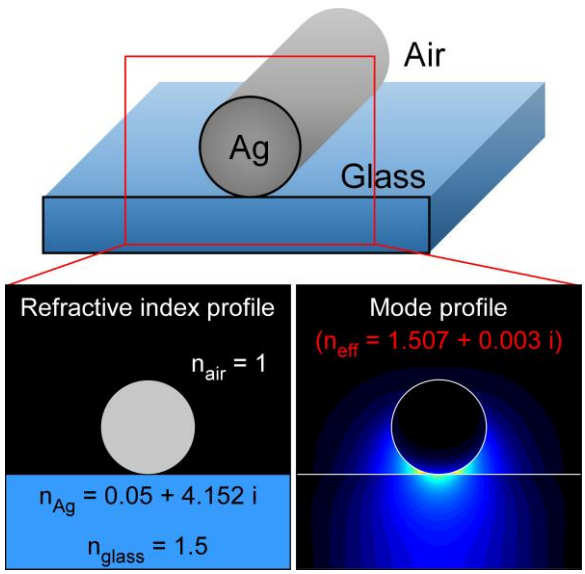

Figure 3. Eigenmode profile at 470 THz of cylindrical silver nanowire (diameter d = 100 nm) on glass substrate. Finite-difference time-domain method was used for this simulation (FDTD Solutions, Lumerical Inc.). The refractive index of silver was taken from Johnson and Christy.[17]

1.2.3. Visualization of SPPs in Metal Waveguides

In general cases, highly confined electric field on the surface of metal waveguide generated from SPPs cannot be collected by lens because SPPs only remain at near-field region. To visualize electric field on the metal surface, it needs to be converted from near-field to far-field area.

Two kinds of microscopy techniques are well-established. The first one is fluorescence-based technique, and the second is tip-based technique.

1.2.3.1. Fluorescence-based Microscopy

If plasmonic structure is coated with fluorescent particles, they can feel SPPs and convert the near field to far-field fluorescence radiation. Hong et al.[10][18] demonstrate that Quantum dots coating which is separated from the surface of silver nanowire by Al_2O_3 dielectric coating can visualize the near-field distribution originated from plasmon beating between two eigenmodes. Also, the shape of those near-field distribution can be tuned by controlling diameter of nanowire, or thickness of dielectric layer, which is similar to theoretical expectation.

These fluorescence-based microscopy takes advantage of excellently high quantum yield of fluorescence process. However, it may suffer from photoblinking[19], photobleaching[20], and

fluorescence quenching[21] by metal surface.

1.2.3.2. Tip-based Microscopy

Tip-based microscopy technique, i.e. scanning near-field optical microscopy (SNOM), uses narrow tip or metal-coated fiber taper to scatter the evanescent waves at near field and convert it to far-field area.[1] The technique can break far-field resolution limit by exploiting the properties of evanescent waves. Therefore, the resolution of images can be limited only by the diameter of the aperture (or the apex of tip), which is below the Abbe's diffraction limit ($d = \lambda / 2n \sin\theta$). In particular, lateral resolution of 20 nm and vertical resolution of 5-10 nm have been reported. [1][22]

However, this technique may hardly be applied to narrow gap-structure smaller than the apex of the tip. If the tip can't approach to inside of the gap, highly confined electric field at the gap will not be resolved.[22]

1.3. Surface-enhanced Raman Scattering

1.3.1. Raman Effect

Raman scattering, or Raman spectroscopy is a branch of vibrational spectroscopy used to investigate vibrational, phonon, and other low-frequency modes in a system. [23] [24]

The (vibrational) Raman effect occurs when light impinges upon a molecule and interacts with the vibrational modes of that molecule. For the spontaneous Raman effect, a photon collides with a molecule and excites it from the initial ground state to a virtual energy state. When the photon is scattered away from the molecule, the molecule relaxes and returns to a different vibrational state. The difference in energy between the original state and this new state leads to a shift in the scattered photon's frequency away from the excitation wavelength. (see figure 4)

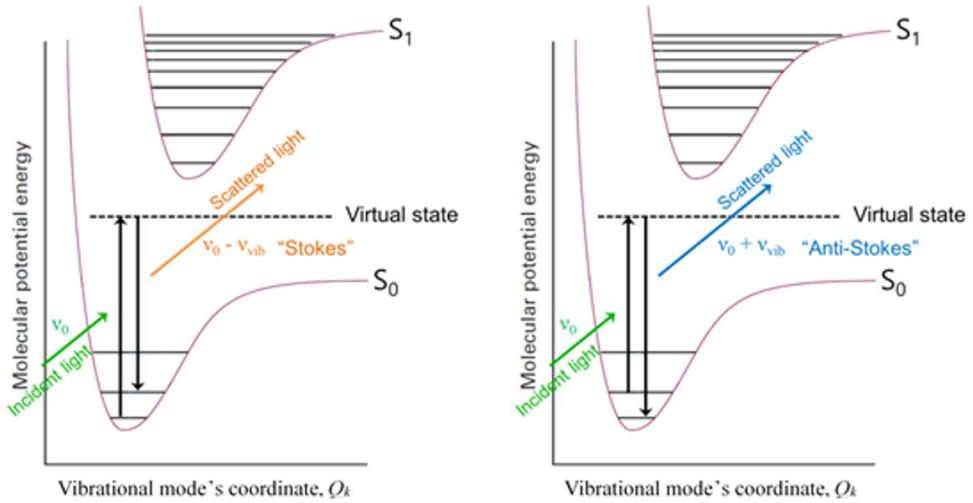

Figure 4. Jablonski diagram related to Raman scattering. (Left) Stokes shift, (Right) Anti-stokes shift.

A change in the molecular polarizability, or the amount of deformation of electron cloud for each vibrational mode, which is described by Raman tensor, determines the Raman scattering intensity. The peak positions in the vibrational Raman spectrum is determined by vibrational frequencies of the target molecule.

1.3.2. Surface-enhanced Raman Scattering

Surface-enhanced Raman spectroscopy (SERS) was discovered in 1974 by three scientists (Hendra, Fleischmann, and McQuillan) at Southampton University.[25] In their initial experiments, they discovered that the Raman spectra of adsorbed on a silver electrode showed unusual strong Raman scattering intensity. Experimental

investigation from multiple research groups showed that there are two underlying mechanisms behind this Raman enhancement[26][27].

The first mechanism which is called as electromagnetic enhancement[26] is the general and dominant effect and occurs due to the enhancement of the electromagnetic field near the molecule of interest. This electromagnetic enhancement is caused by the interaction between the electromagnetic field and a nearby plasmonic substrate. The second form of enhancement is called as chemical enhancement[27] and is a result of the other chemical phenomena, for instance, a change in polarizability induced by molecule–metal bond formation, and preference for specific orientation of molecule.

1.3.3. Electromagnetic Enhancement

Lastly, we briefly look through the process of the electromagnetic enhancement for metal nanoparticle dimer cases as a generic SERS substrate.[28][29] The electromagnetic enhancement is generally explained as combination of two individual steps.[30]

The first step is called as 'Plasmon excitation step'. When the incident light of wavelength ranged from near–IR to visible hits plasmonic nanostructure, for instance nanoparticle dimer, localized surface plasmon resonance (LSPR) will occurs on it. This LSPR generates extremely enhanced local electric field at specific sites, for example, sharp corner or narrow gap of nanostructure. In general, we call these sites as '(Plasmonic) Hotspots'. In plasmonic

excitation step, the enhancement of local field ($|E|^2/|E_0|^2$) at hotspots generally ranges from 10^2 to 10^4.

In the second step which is called as 'Raman emission step', Raman probes near hotspots which excited by the enhanced local field emits Raman scattered photons. Also, these photons excite LSPR of the nanostructure once again. In this case, the frequency of LSPR is equal to that of Raman shifted photons. This LSPR mode, especially, can be treated as oscillating dipole, which emits some radiation to far-field region. Therefore, Raman emission from the Raman probes can be enhanced by radiative LSPR mode of nanostructure.[30] [31] (see figure 5)

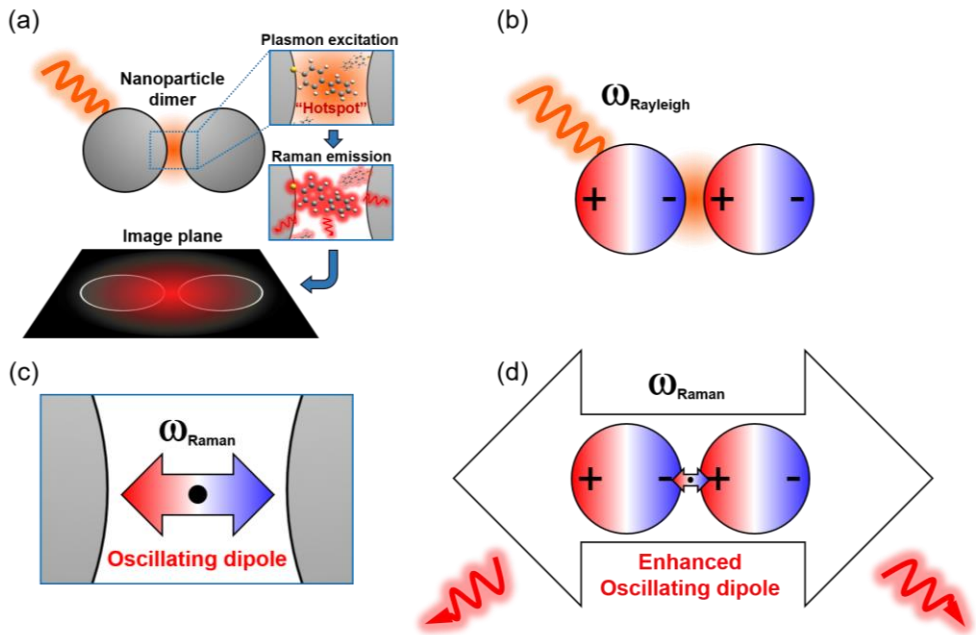

Figure 5. (a) Overview of electromagnetic enhancement. (b) Plasmon excitation caused by incident light with frequency $\omega_{Rayleigh}$. (c) Following Raman emission of a molecule near the gap. (d) Enhanced Raman emission of plasmonic structure.

1.4. Goal of the project

Compared to fluorescence-based techniques, SERS is relatively free from fluorescence quenching[21], photoblinking[19] and photobleaching[20].

Furthermore, compared to tip-based techniques, SERS takes advantage of using small organic molecules as Raman probe so that confined plasmon at narrow gap can be effectively resolved.

To verify this idea, we applied SERS imaging technique for visualizing SPPs at gap of silver nanowire dimer. Here, we can suggest two important questions, described below. (schematically illustrated in figure 6)

Q1) Can SERS imaging visualize SPPs at one-dimensional hotspots?

Q2) What's the difference between NP and NW dimer as SERS substrate?

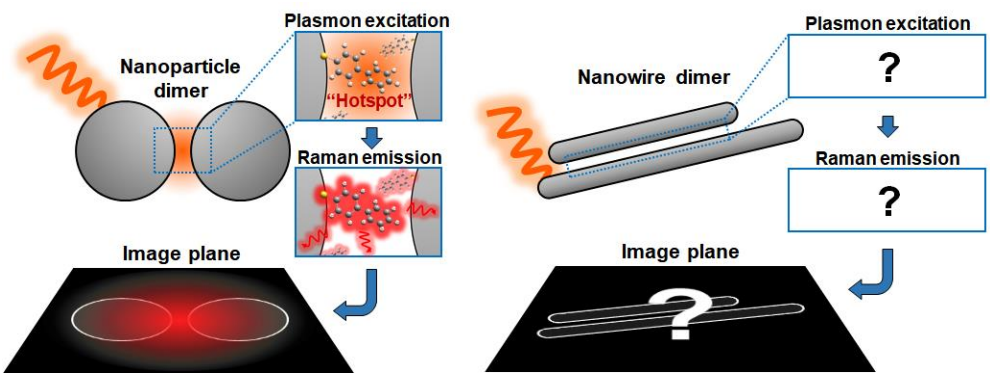

Figure 6. Schematically illustrated concepts of SERS imaging of silver nanowire dimer.

2. Experimental Setup

2.1. Confocal Raman Microscope System

SERS imaging, which combines Surface-enhanced Raman spectroscopy and microscopic imaging techniques, is an excellent method for obtaining information about the spatial distribution of chemical species.

The linearly polarized excitation light from a 632.8 nm HeNe laser or an 532 nm ND:YAG laser is delivered into the entrance port of the inverted confocal microscope through a Raman dichroic beam splitter, and focused on the sample surface by an oil-immersive objective lens (1.4 NA, oil-immersion type, U Plan S-Apo, Olympus co.). The polarization of incident beam can be tuned by 632.8 nm or 532 nm half-wave plate. After beam focused to the sample plane, the same objective lens collects the Raman signal in the epi-direction. The back-scattered Rayleigh radiation is also collected and rejected by two optical filters (a Raman edge-filter, and a Raman notch-filter) placed in front of a monochromator-EMCCD system (Shamrock 500i monochromator, ANDOR Technology LTD. / iXon3 897 512 x 512 pixel, -90 ℃ TE-cooled EMCCD, ANDOR Technology LTD).

The angle of the grating mirror which is loaded in monochromator can be tuned as the zero order, or the first order. The zero order grating acts like mirror, which achromatically

reflects image plane onto EMCCD plane. On the other hand, the first order grating reflects image with specific angle defined by Bragg's law, regarding its wavelength. Therefore, we can obtain SERS and Rayleigh image (confocal spectrum), when the zero order (the first order) grating is used.

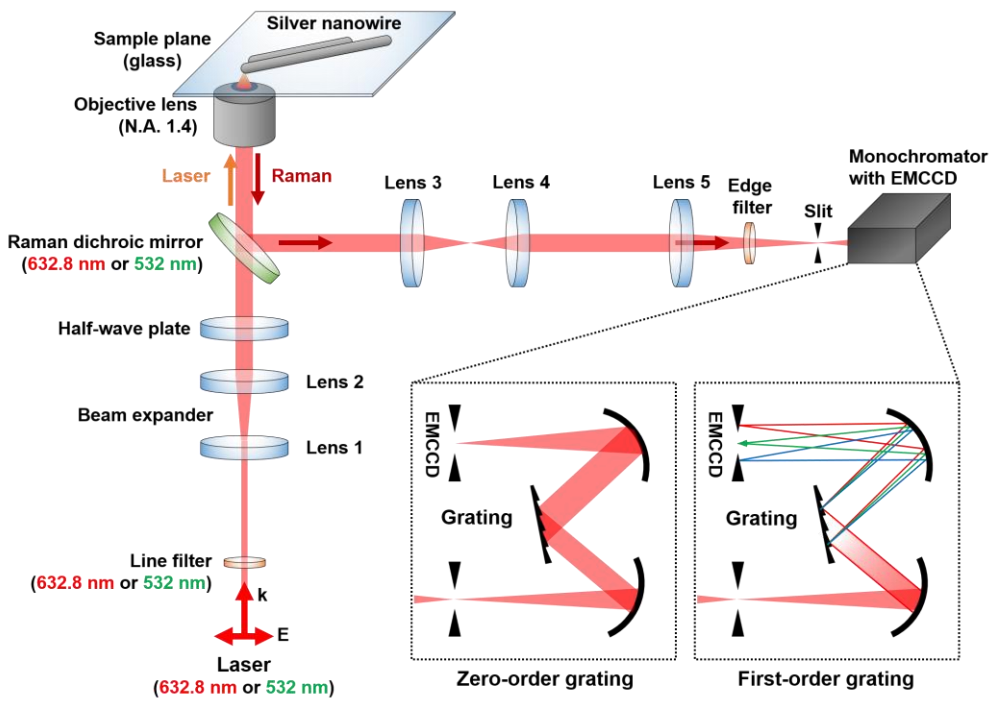

Figure 7. Schematic diagram of the entire experimental system. (see the details in main text)

3. Direct Visualization of Silver Nanowire Dimers using SERS

3.1. Sample Preparation

3.1.1. Polyol Synthesis of Silver Nanowires

Single-crystal colloidal silver nanowires (AgNWs) is synthesized by slightly modified polyol process from Coskun et al.[32]. In a typical synthetic process, all glassware used in the experiments were cleaned with aqua regia solution, alconox, and finally deionized water (18.3 MΩ). All chemicals were purchased from Sigma-Aldrich and used without further purification. In a typical synthesis process, 10 mL of 0.3 M ethylene glycol (EG) solution of polyvinyl pyrrolidone (PVP, MW 55000) was prepared and 7 mg of NaCl (99.5%) was added into the solution. During reflux the PVP/EG solution in 100 mL-sized round bottom flask at 170 °C, 5 mL of 0.12 M $AgNO_3$/EG solution was freshly prepared. Then, $AgNO_3$/EG solution was added dropwise into the refluxed PVP/EG solution using syringe at a rate of 5 mL/h. The solution was stirred at a rate of 1000 rpm by a magnetic stirrer during the whole process. As Ag^+ ions were injected into PVP/EG solution, Ag seeds start to form via homogeneous nucleation. Upon the completion of dropwise addition, the nanowire solution was annealed for additional 30

minutes at 170 °C and finally air-cooled to room temperature.

Then, the solution was incubated in refrigerator for 48 hours to separate heavy AgNWs and light Ag seeds by decanting. After separation, precipitation of AgNWs was washed with anhydrous ethanol 9-10 times, and finally redispersed in 9 mL ethanol. The purified AgNWs solution was stored in refrigerator.

The average diameter of purified AgNWs, which is measured from AFM topographies, was 165.2 nm (std. deviation 52.1 nm). Also, It is well known that cross section of AgNW is mostly pentagonal shape.[33]

3.1.2. Surface Modification of Silver Nanowires

In Liang et al.[34], it was reported that PVP coated AgNWs can be readily modified with small thiol molecules. Therefore, carefully chosen thiol molecules, in this case biphenyl-4-thiol (BPT), can be used as both PVP-stripping agents and Raman probes.

After purification process, the AgNW solution was diluted for 5 times with ethanol. Then, 0.2 mL of 10 mM BPT ethanolic solution is injected into 1 mL of diluted AgNW solution. After 24 hours, AgNWs were washed 5 times with methanol and redispersed in 1 mL of methanol.

As an evidence for surface modification, figure 8, shows that colloidal stabilities of PVP-coated or BPT-coated AgNW colloids in water are significantly different, which means that BPT-coated AgNWs have hydrophobic surfaces due to biphenyl moiety on them.

Finally, a drop of 5 mL of the purified BPT-coated AgNW methanolic solution was drop-casted on glass coverslip using micropipette and dried in atmosphere. After solvents is evaporated, AgNWs on glass substrate can be roughly characterized using conventional optical microscope (Leica upright microscope).

In the end, after SERS imaging experiment, AFM (XE-80, Park systems) topographies of the same sample is measured to specify spatial dimension of NW dimer.

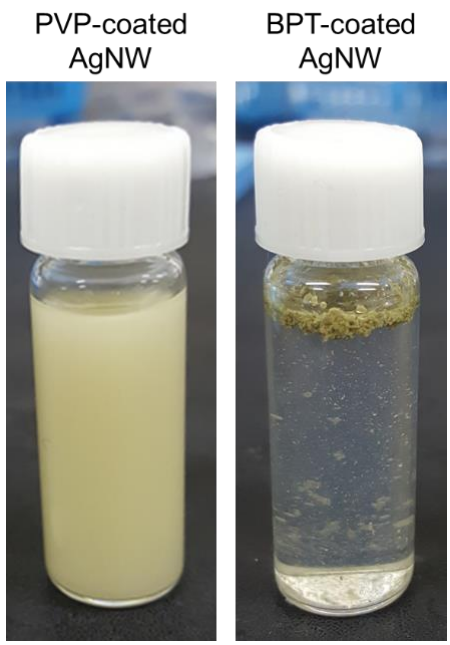

Figure 8. (Left) Colloid solution of PVP-coated AgNW in H_2O. (Right) Colloid solution of BPT-coated AgNW in H_2O

3.2. Wide-field SERS Imaging for Silver Nanowire Dimers

As depicted in figure 9, tightly focused laser beam (λ_{ex} = 632.8 nm or 532 nm) on the protruding end point from AgNW dimer can launch SPP along NW-axis. If plasmonic hotspots are generated in the gap of AgNW dimer by gap-mode SPP, we will collect Raman emissions from BPT monolayer coated on AgNW surface. Arranging edge filter in front of detector as illustrated in figure 7, Rayleigh scattering signal is filtered out so that we can collect only SERS signal. Thus, we can obtain a wide-field SERS image taken from AgNW dimer as illustrated in figure 9. Also, SERS spectrum of BPT measured from the same AgNW dimer is shown. Note that BPT is non-resonant Raman probe at λ_{ex} = 632.8 nm or 532 nm, so that spectrum with very low background intensity is obtained. Therefore, we can hypothesize that three SERS peaks (1089 cm^{-1}, 1291.7 cm^{-1}, 1611 cm^{-1}) mainly contribute to generation of the image plane. In addition, Theoretical Raman spectrum of BPT attached to single Ag atom is also depicted as red lines which referred to pick positions and intensities. (DFT calculation using Gaussian09 package[35] based on B3LYP (Becke, three-parameter, Lee-Tang-Parr)/6-311++ G(d, p))

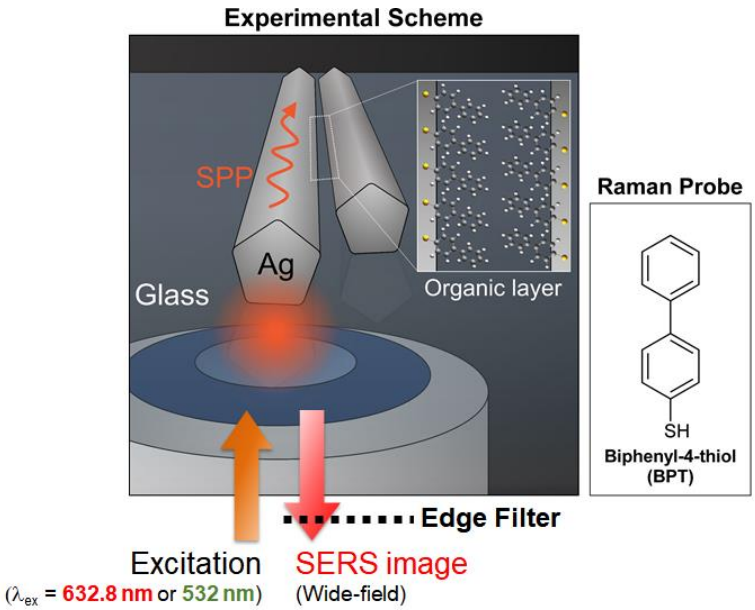

Figure 9. Experimental scbeme for wide-field SERS imaging on AgNW dimers.

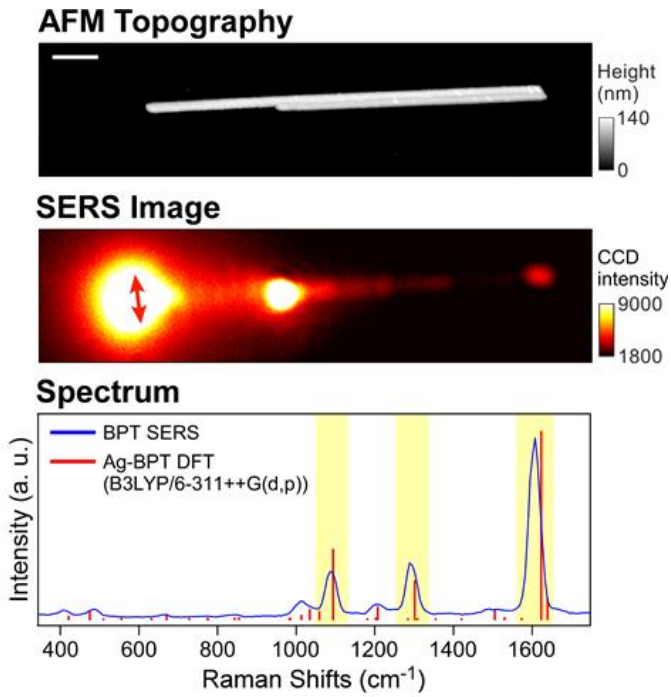

Figure 10. Typical example of SERS at AgNW dimer. (upper) AFM topography of AgNW dimer. (middle) wide-field SERS image (λ_{ex} = 632.8 nm). (bottom) Experimental and theoretical SERS spectrum of BPT coated on AgNW dimer surface.

In figure 11 and 12, SERS and Rayleigh images which are measured from the same sample with excitation wavelength λ_{ex} = 532 nm and 632.8 nm are shown. Firstly, we can compare the SERS images to the Rayleigh images. It can be noticed that only the SERS images have oscillating intensity patterns along their NW-axis. The Rayleigh images only have simple decay patterns and fine interference patterns along NW-axis.

The patterns in Rayleigh images look like leakage microscopy images from previously reported papers[13][36]. In leakage microscopy for SPPs at silver nanowire monomer, only few higher-order eigenmodes with low effective index can be leaked through substrate of high refractive index. In other words, if the leakage microscopy image is obtained for one-dimensional waveguide, we can obviously vindicate the existence of higher-order eigenmodes. Therefore, the AgNW dimer in figure 11, and 12 is multi-mode plasmonic waveguide.

For the next step, we can set the excitation wavelength λ_{ex} as the comparison point between SERS images. Comparison between SERS images of λ_{ex} = 532 nm and 632.8 nm tells us that periodicity of the oscillating patterns increases as excitation wavelength increases. Secondly, the overall propagation length increases.

Finally, we can compare them with the polarization of the focused incident laser beam. When the transverse polarization is changed to longitudinal, local maxima in SERS image of λ_{ex} = 632.8 nm before defect of AgNW, are shifted.

These oscillating patterns may be derived from lightning rod effect caused by surface defects (or surface roughness) on silver nanowires, Fabry-Perot resonance[37] and Plasmon mode beating[18]

(see figure 13). At least, we can hypothesize that surface roughness does not take part in the major contribution because of the polarization dependence of the phase and the excitation wavelength dependence of the periodicity in the oscillating image.

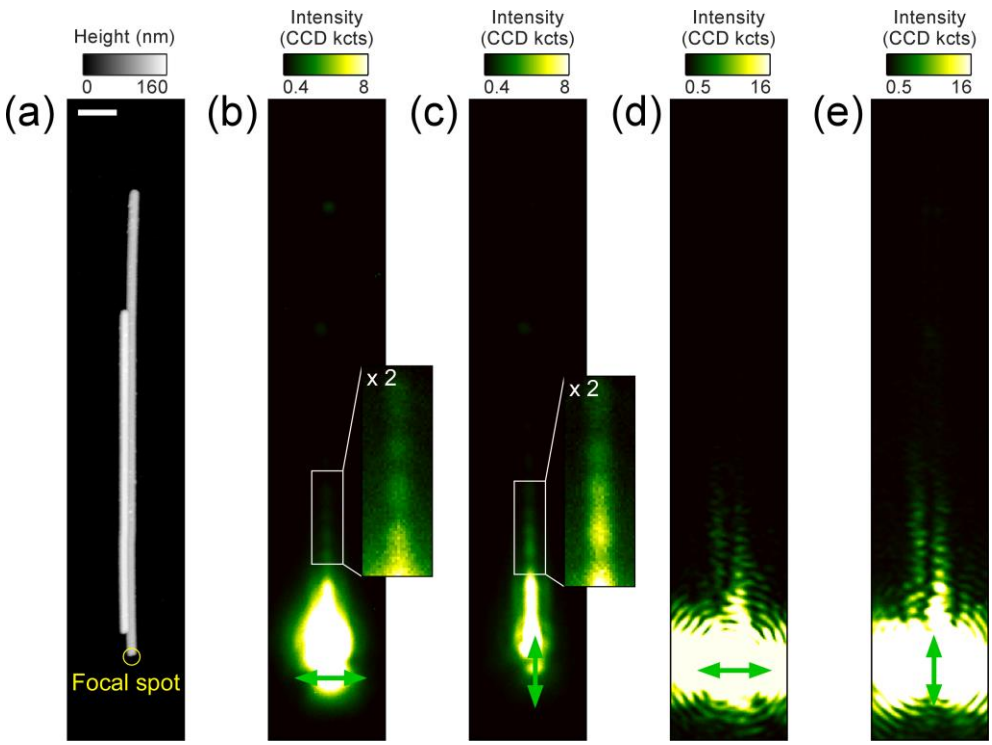

Figure 11. Experimentally measured SERS and Rayleigh images. **(a)** AFM topography of silver nanowire dimer. (scale bar = 1 μm) **(b, c)** SERS images (λ_{ex} = 532 nm). **(d, e)** Rayleigh images (λ_{ex} = 532 nm). The inset shows magnified images with doubly enhanced color scale. All the arrows in each image refers to polarization of excitation laser.

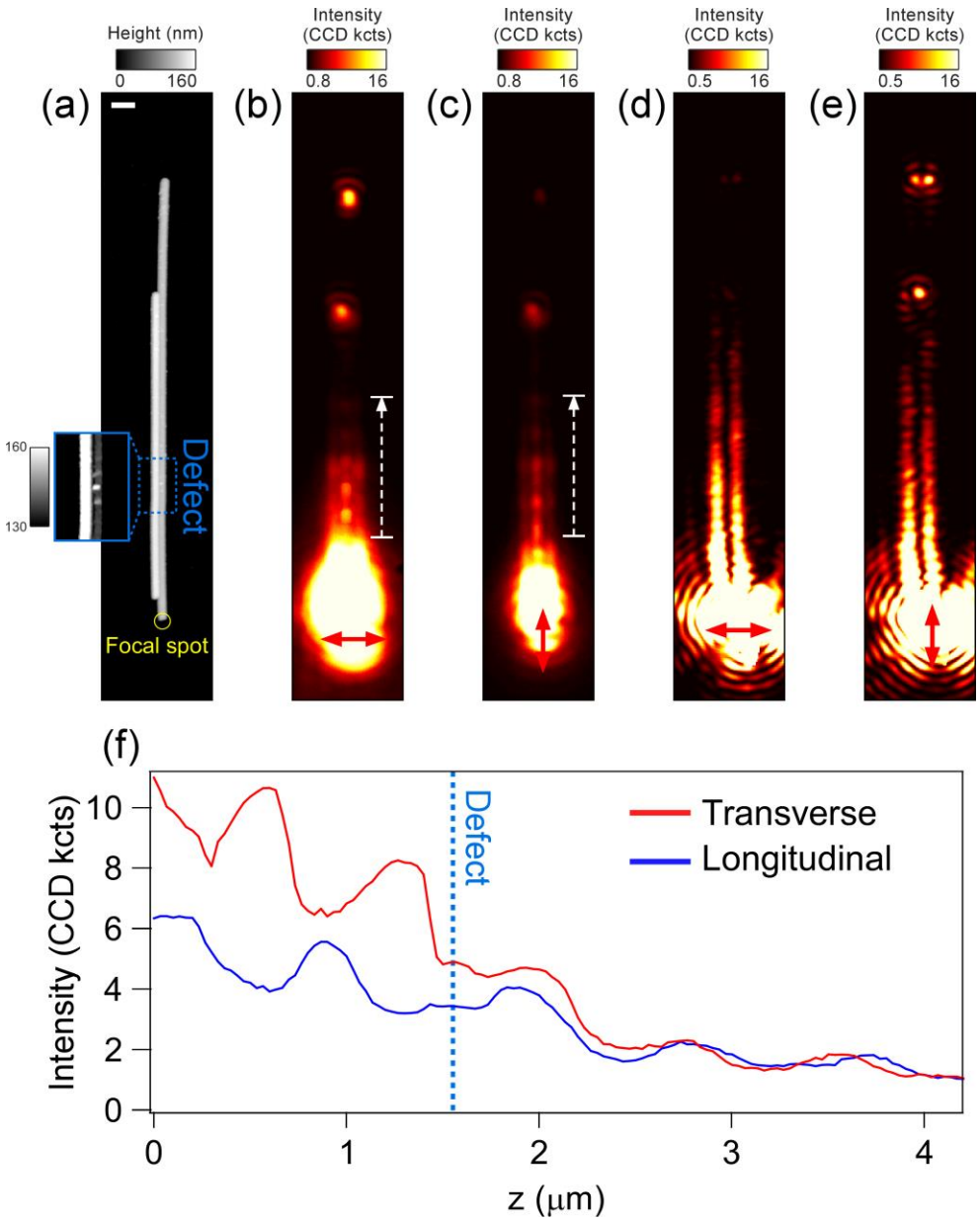

Figure 12. Experimentally measured SERS and Rayleigh images. **(a)** AFM topography of silver nanowire dimer. (scale bar = 1 μm) The inset shows magnified image near defect at AgNW. **(b, c)** SERS images (λ_{ex} = 632.8 nm). **(d, e)** Rayleigh images (λ_{ex} = 632.8 nm). Inset represents magnified images with doubly enhanced color scale. All the arrows in each image refers to polarization of excitation laser. **(f)** SERS intensity profile along NW−axis depicted in (b, c).

3.3. Finite Difference Time Domain Simulation

3.3.1. Near-field Simulation

To find the origin of these behaviors of the oscillating patterns, we tried to use simulation based on electromagnetic theory. Finite difference time domain (FDTD) Maxwell solver (*FDTD Solutions*, Lumerical Inc.) was chosen for simulating the plasmon excitation step in electromagnetic enhancement of SERS phenomenon.

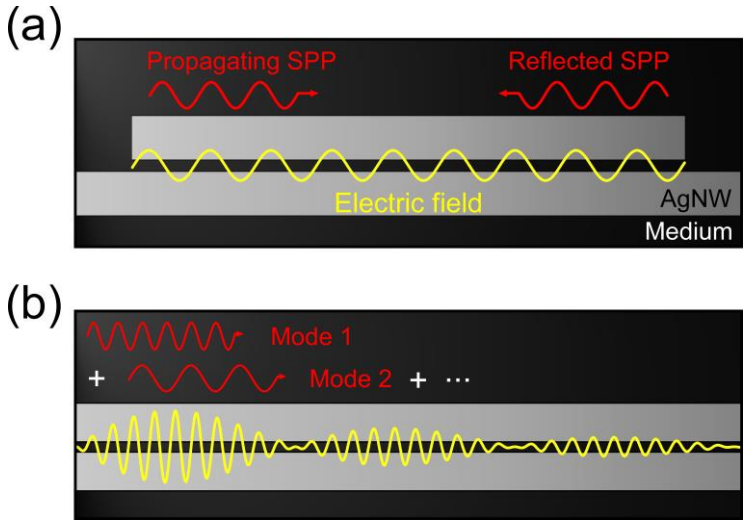

Figure 13. Schematic illustration of **(a)** Fabry-Perot resonance and **(b)** Plasmon mode beating effect.

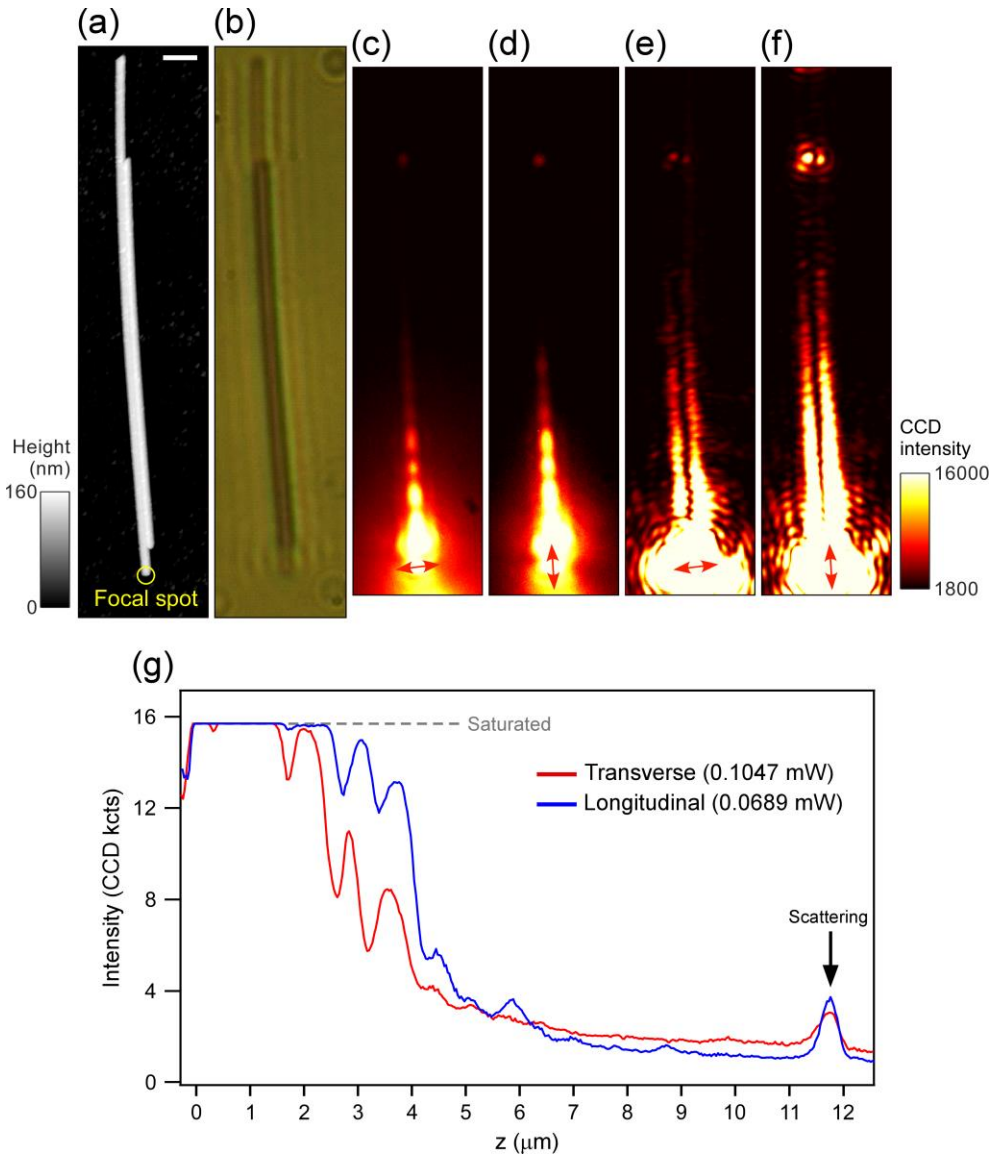

Figure 14. An example of SERS images and their line profiles along NW−axis. **(a)** AFM topography of AgNW dimer. (scale bar = 1 μm) **(b)** Transmission optical image measured from CMOS camera. **(c)** SERS image excited by 632.8 nm focused laser beam with transverse polarization. **(d)** SERS image excited by 632.8 nm focused laser beam with longitudinal polarization. **(e)** Rayleigh image excited by 632.8 nm focused laser beam with transverse polarization. **(f)** Rayleigh image excited by 632.8 nm focused laser beam with longitudinal polarization. **(g)** SERS intensity profile along NW−axis, obtained from (c,d)

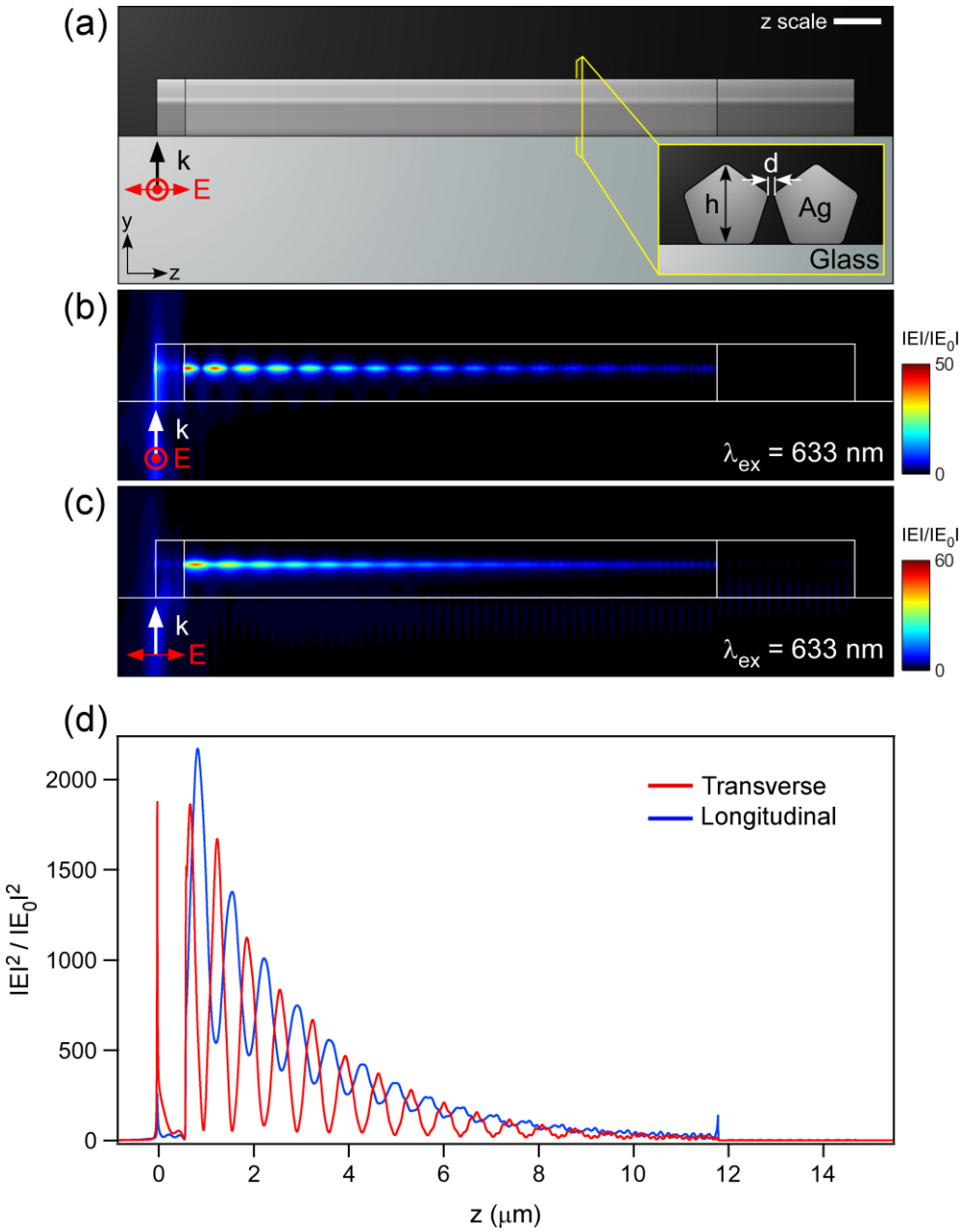

Figure 15. Simulated near-field distribution at gap of AgNW dimer modelled from AFM topography in figure 12. **(a)** Illustration for model structure. (height = 150 nm, corner radius = 15 nm, gap distance = 5 nm, and scale bar = 1 μm) **(b)** Simulated near-field distribution at gap of AgNW dimer excited by transverse polarization. **(c)** Simulated near-field distribution at gap of AgNW dimer excited by longitudinal polarization. **(d)** Squared line profiles from (b) and (c).

First, we tried to figure out whether FDTD simulation can represent the oscillating pattern of near-field distribution at gap of AgNW dimer. In figure 14, an example of SERS images and their line profiles along NW-axis are shown. Based on AFM topography of the AgNW dimer, virtual structure can be modelled in FDTD simulation. The modelled structure is depicted in figure 15. AgNW dimer which has refractive index value referred from Johnson and Christy[17] is on the glass substrate with refractive index 1.5. The height of the AgNW dimer is 150 nm, based on AFM topography. We can simulate a focused laser beam on the AgNW's terminus with gaussian beam (NA = 1.4, incident from glass substrate) of specific wavelength. Parameterizing the gap distance between the two AgNWs, we found that 5 nm gap distance provides 600 - 700 nm sized periodicity at the gap of AgNW dimer.

The simulated near-field distribution obviously has the characteristics which was shown in SERS images. In figure 15, the squared line profiles of near-field distribution ($|E|^2/|E_0|^2$) is depicted and it is noticeable that the phase shift occurs between the two input polarizations of the gaussian beam. In figure 16 and 17, total simulation results for full wavelength of visible range are shown. As we can see, this simulation also successfully represents propagation length change and periodicity change. In this step, we can conclude that the origin of the oscillating patterns in SERS images is derived from the plasmon excitation step in SERS electromagnetic enhancement.

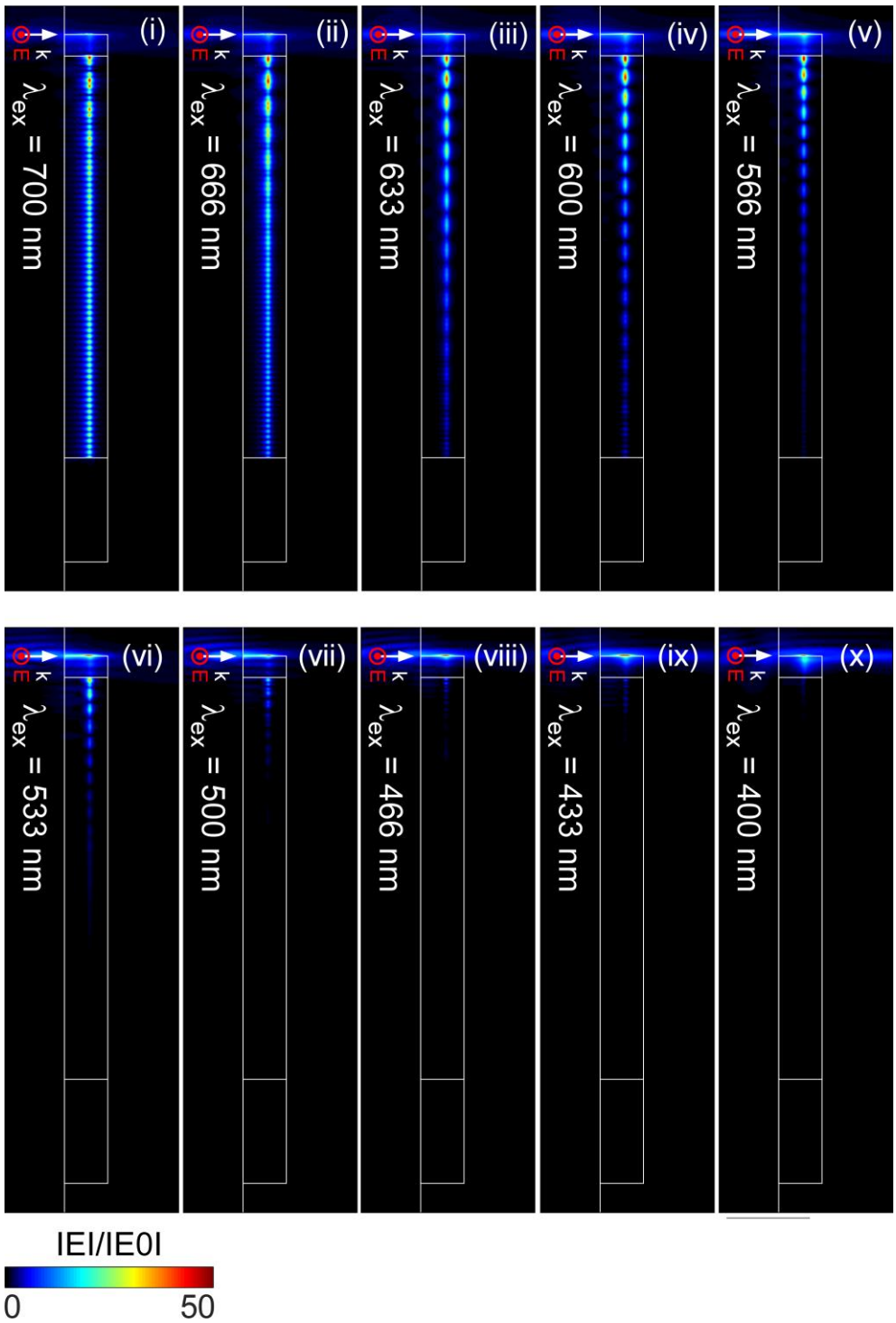

Figure 16. Simulated near-field distribution at the gap of AgNW dimer (gap size d = 5 nm) excited by gaussian beam of transverse polarization.

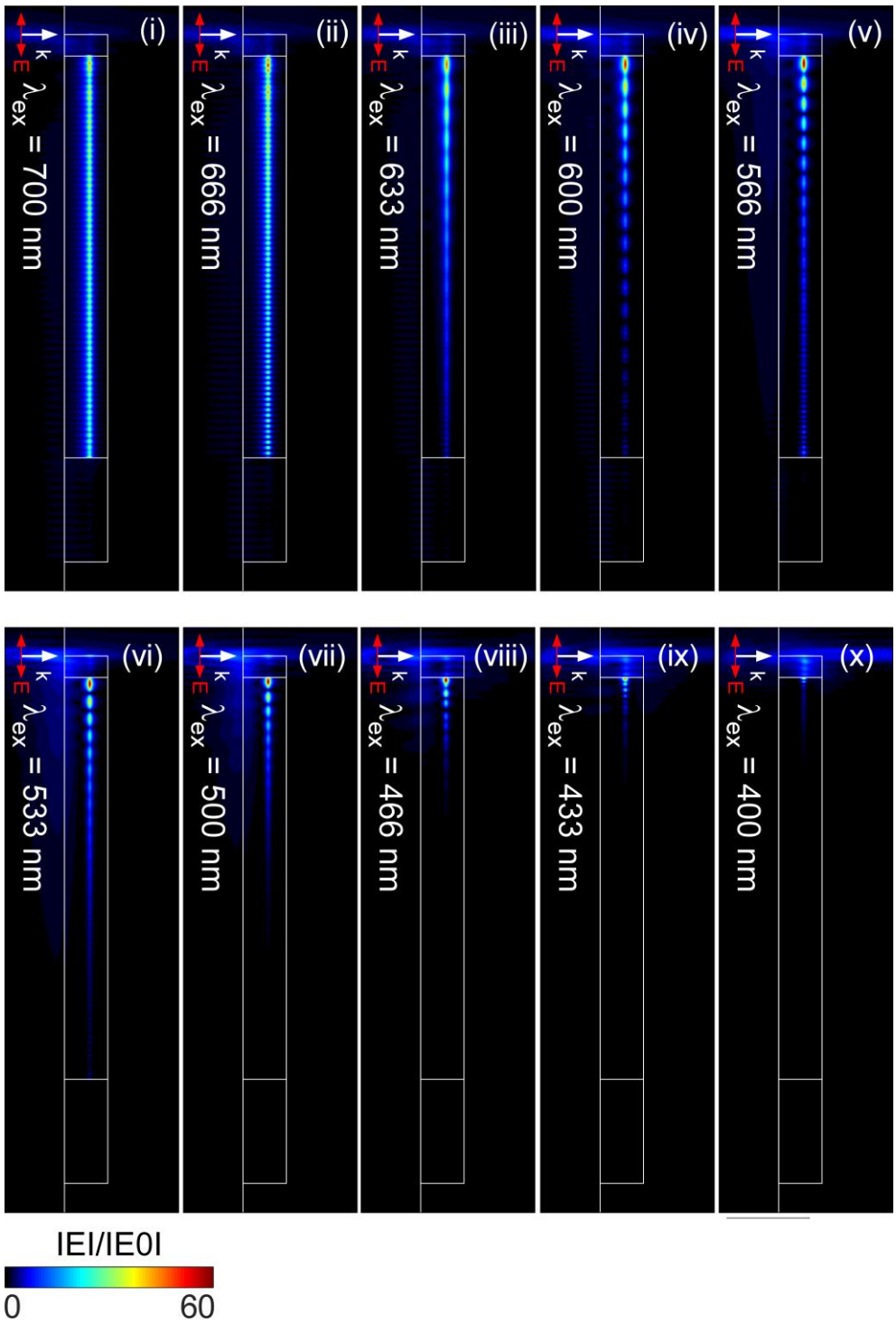

Figure 17. Simulated near-field distribution at the gap of AgNW dimer (gap size d = 5 nm) excited by gaussian beam of longitudinal polarization.

For the next step, we need to figure out how the oscillating near-field pattern arises. As explained before, we can think the two candidates as the origin, Fabry-Perot resonance and plasmon mode beating. If the oscillating near-field pattern is derived from Fabry-Perot resonance, the pattern will not appear for infinitely elongated AgNW dimer structure. Therefore, we can build those infinite structure in FDTD simulation and launching SPPs of several eigenmodes. If the oscillating pattern arises, we can conclude that those spatially modulated pattern is derived from plasmon mode beating effect.

In figure 18, the model structure which has infinite AgNW monomer part as its half part, and AgNW dimer part as its the other half part is depicted. Several eigenmodes at monomer part which are illustrated in figure 19 are injected one at a time toward dimer part, and converted to summation of eigenmodes of dimer part. Then, the electric field at specific cross section is analyzed by eigenmodes in figure 20 as basis set.

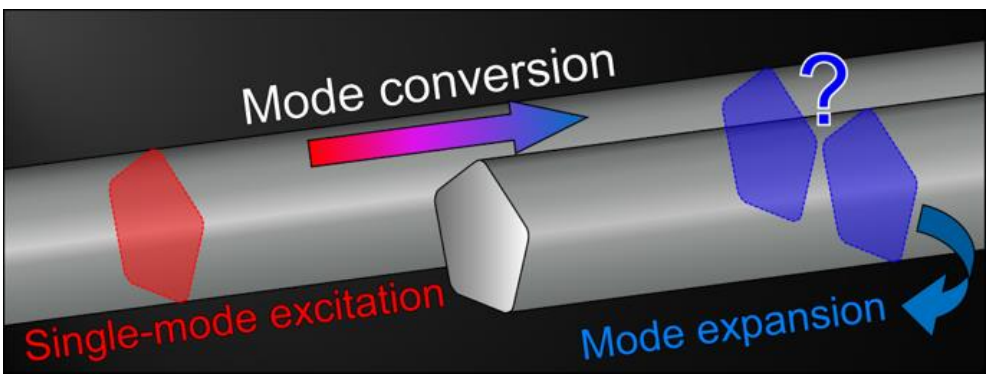

Figure 18. Model structure for mode analysis simulation. The overall dimension of AgNW structure is the same as model depicted in figure 13, except existence of glass substrate. To supplement this ignorance of glass substrate, background index is set to 1.25 which is average value between those of air and glass.

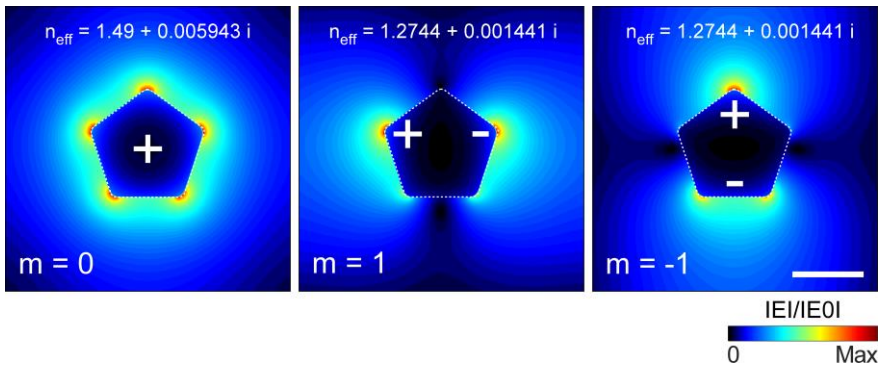

Figure 19. Electric field distribution of each eigenmodes at AgNW monomer and their effective index values. The mark '+, −' means to the sign of charge density in cross section of AgNW. The index 'm' refers to the angular momentum of each eigenmode.

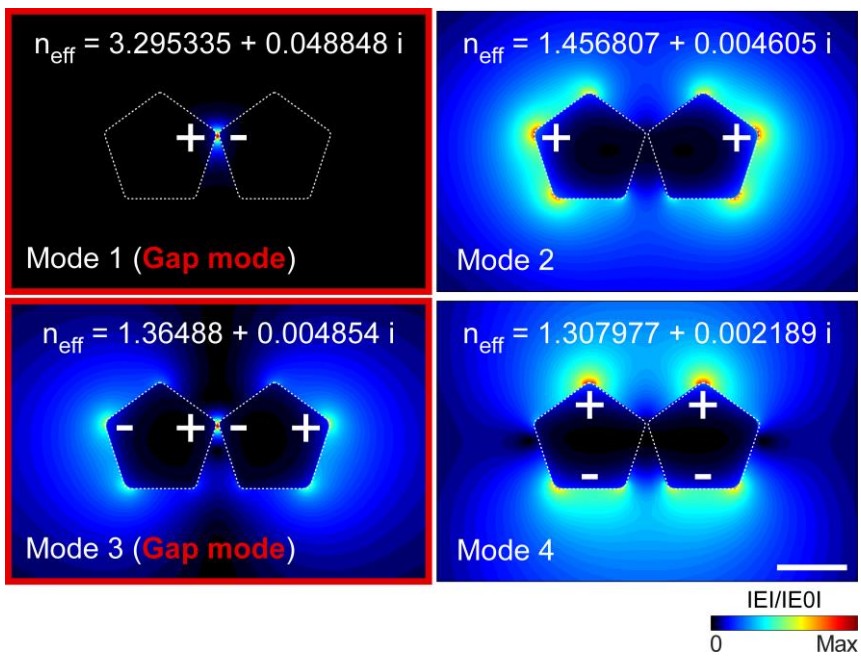

Figure 20. Electric field distribution of each eigenmodes at AgNW dimer and their effective index values. The mark '+, −' means to the sign of charge density in cross section of AgNW. The two gap modes, mode 1 and 3, especially have opposite sign of surface charge density so that these modes have highly localized electric field at the gap.

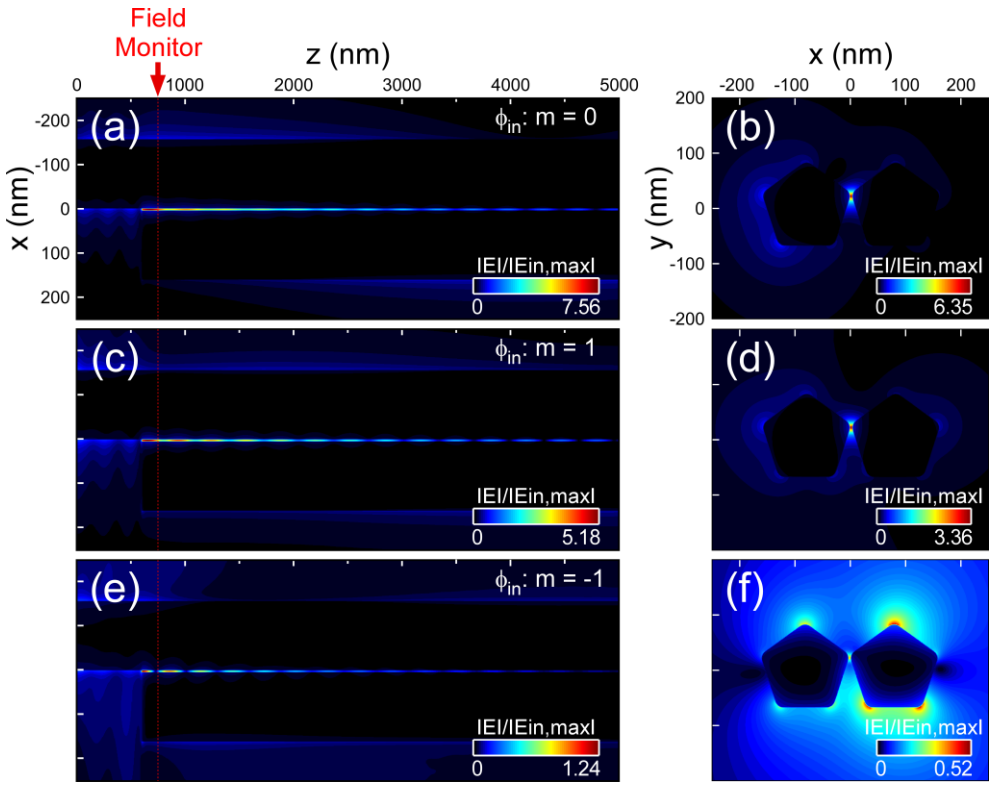

Figure 21. Near-field distribution excited by specific single mode excitation at monomer part. **(a, c, and e)** Electric field distribution at the gap along NW-axis. **(b, d, and f)** Electric field distribution of cross section taken from the position marked by red arrow.

Being excited by single eigenmode of monomer at z = 0 nm, the electric field pattern formed at the gap of dimer arises. For m = 0 and m = 1 as input eigenmode, the oscillating pattern occurs. As already described, there is no reflected SPPs at AgNW dimer in this system so that we can conclude that Fabry-Perot resonance does not take part in major contribution for generating oscillating near-field pattern. On the other hand, m = −1 input seems to excite non-gap modes (mode 2 or mode 4 in figure 20).

Before looking on mode expansion result, we need to understand the concept of mode expansion briefly. Consider a

waveguide that supports a set of forward-propagating SPP modes, ϕ^{f}_{m} (with electric field E^{f}_{m} and magnetic field H^{f}_{m}), and backward-propagation modes, ϕ^{b}_{m} (with E^{b}_{m} and H^{b}_{m}). If we know the complete basis state of modes, we can analyze the input field using the basis:

$$\vec{E}_{in} = \sum_{m} (a_m \vec{E}^{f}_{m} + b_m \vec{E}^{f}_{m}) \quad \text{(Eq. 8)}$$

$$\vec{H}_{in} = \sum_{m} (a_m \vec{H}^{f}_{m} + b_m \vec{H}^{f}_{m}) \quad \text{(Eq. 9)}$$

a_m and b_m represent the complex transmission coefficient of the forward and backward propagating eigenmodes respectively. The forward and backward propagating modes are related as below.

$$\vec{E}^{b}_{m} = \vec{E}^{f}_{t,m} - \vec{E}^{f}_{z,m} \cdot \hat{z} \quad \text{(Eq. 10)}$$

$$\vec{H}^{b}_{m} = -\vec{H}^{f}_{t,m} + \vec{H}^{f}_{z,m} \cdot \hat{z} \quad \text{(Eq. 11)}$$

Note that we decomposed $E^{f}_{t,m}$ in a transverse component (along x and y) and longitudinal component $E^{f}_{z,m}$ (along propagating direction z), and similarly for H^{f}_{m}. Thus, we can summarize the expression above for the input fields in terms of forward-propagating modes. Then, we can omit the 'forward (f)/backward (b)' notation and write each eigenmode as ϕ_m (with E_m and H_m) for the forward-propagating modes. If we assume power orthogonality between these eigenmodes, we can an equation for overlap integral of Poynting vector between two eigenmodes as below:

$$\langle \phi_m | \phi_n \rangle = \frac{1}{2} \int dS \cdot \vec{E}_m \times \vec{H}^{*}_{n} = N_m \delta_{mn} \quad \text{(Eq. 12)}$$

Then the coefficients for any mode m in input field can be determined from the overlap integrals:

$$\frac{1}{2}\int dS \cdot \vec{E}_{\mathrm{in}} \times \vec{H}_{\mathrm{m}}^{*} = (a_{\mathrm{m}} + b_{\mathrm{m}})N_{\mathrm{m}} \qquad \text{(Eq. 13)}$$

$$\frac{1}{2}\int dS \cdot \vec{E}_{\mathrm{m}} \times \vec{H}_{\mathrm{in}}^{*} = (a_{\mathrm{m}} - b_{\mathrm{m}})N_{\mathrm{m}} \qquad \text{(Eq. 14)}$$

This is the basic concept of eigenmode expansion of SPP propagation. For example, input field can be (b), (d) and (f) in figure 21 and eigenmode m can be one in figure 19. Consequently, we can calculate the power of each mode m in the waveguide based on how much each eigenmode takes part in generating input field. The coefficient b_m is zero for all cases because there is no any reflection of SPPs in the model. Thus, we need to solve only a_m value. In the end, we can calculate each parameter and normalized forward transmission (T_m) of eigenmode m:

$$a_{\mathrm{m}} = \frac{1}{4}\left(\frac{\int dS \cdot \vec{E}_{\mathrm{in}} \times \vec{H}_{\mathrm{m}}}{N_{\mathrm{m}}} + \frac{\int dS \cdot \vec{E}_{\mathrm{m}} \times \vec{H}_{\mathrm{in}}}{N_{\mathrm{m}}^{*}} \right) \qquad \text{(Eq. 14)}$$

$$N_{\mathrm{m}} = \frac{1}{2}\int dS \cdot \vec{E}_{\mathrm{m}} \times \vec{H}_{\mathrm{m}} \qquad \text{(Eq. 15)}$$

$$\mathrm{T}_{\mathrm{m}} = \frac{|a_{\mathrm{m}}|^{2} N_{\mathrm{m}}}{\text{Sourcepower at monomer}} \qquad \text{(Eq. 16)}$$

The actual calculation was done using mode expansion monitor in 2D FDTD solver (FDTD Solutions, Lumerical Inc.).

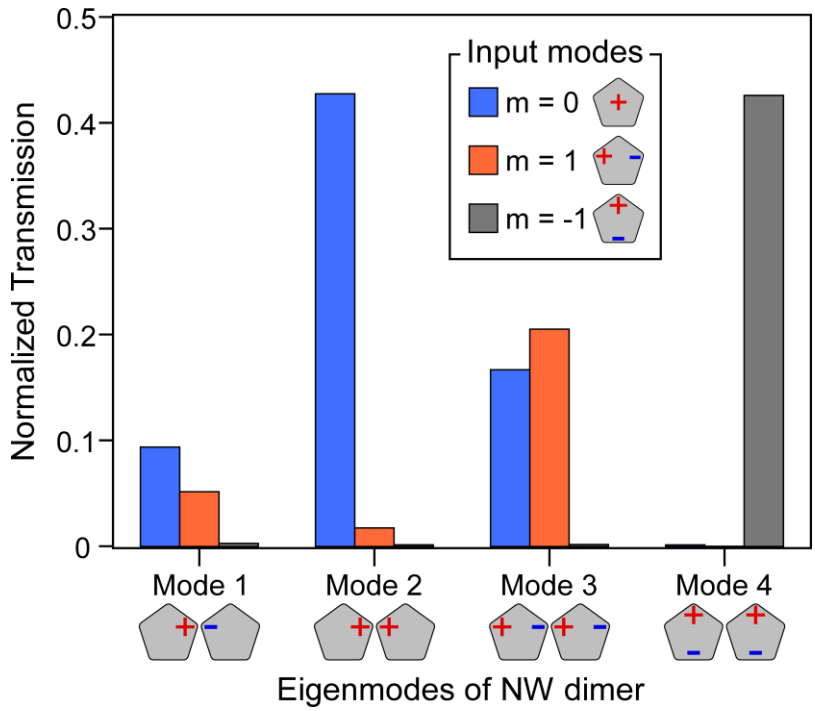

Figure 22. The result of mode analysis. For each input eigenmode (m = 0, 1 and −1), transmission power ratio of each eigenmode of dimer is calculated. It is noticeable that m = 0 and m = 1 is converted mode 1 and mode 3 simultaneously.

In figure 23, mode analysis result is shown. In the plot, x axis refers to each eigenmode of dimer, y axis refers to transmission power ratio of each eigenmode, which is normalized by input transmission. It is noticeable that m = 0 and m = 1 inputs excites both gap modes simultaneously. Therefore, the oscillating patterns in SERS images is originated from plasmon mode beating between two gap modes, mode 1 and 3.

3.3.2. Far-field Simulation

Strictly speaking, the SERS images which are experimentally measured from image plane of Raman microscope may not perfectly equal to near field distribution at AgNW dimer. In the mechanism of electromagnetic enhancement in SERS, photons emitted from Raman emitter excite specific surface plasmon modes. Those excitations of surface plasmon with Raman-shifted frequency can bring enhanced radiation to far-field region. For example, SERS images in figure 12 and 14 exhibit SERS radiation at distal ends of AgNW dimer cannot be explained because the near-field intensity is too weak. Thus, the Raman emission at distal ends obviously comes from molecules near the gap around excitation spot where near-field intensity is large enough. Consequently, Raman emission from those molecules are transmitted as the form of SPP which propagates to distal end of AgNW dimer and finally scattered to far-field region.

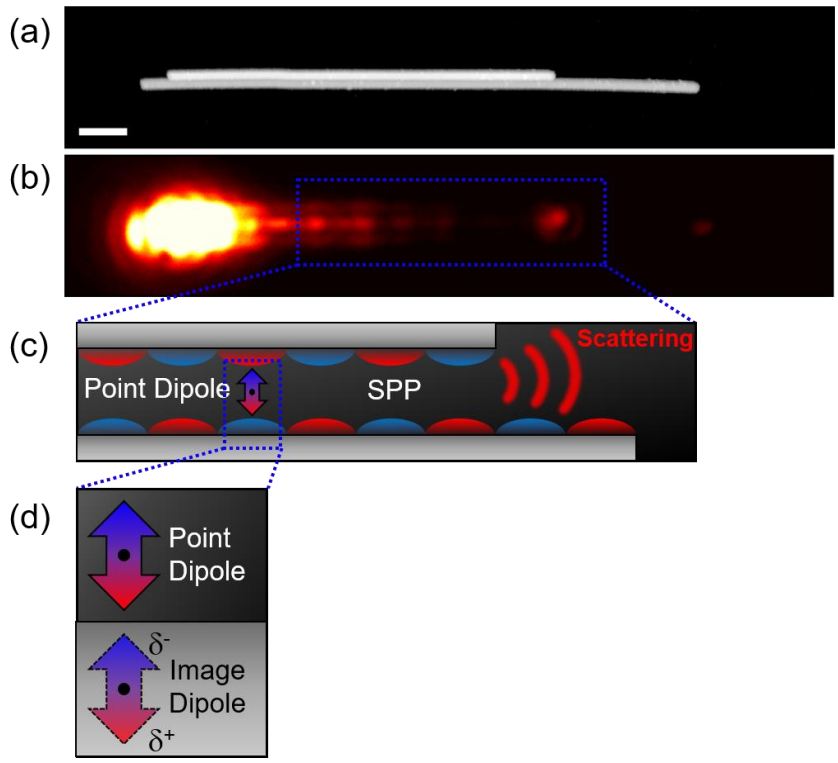

Figure 23. Schematic illustrations of molecule–NW coupling. **(a)** AFM topography of figure xx. **(b)** SERS image at λ_{ex} = 632.8 nm excited by focused beam of longitudinal polarization. **(c)** Point dipole–SPP coupling. **(d)** Point dipole–Image dipole coupling.

Therefore, we need to study extensively the coupling between molecules and nanowire dimer. Then, we can think two types of molecule–NW coupling which are depicted in figure 23. The first is 'Point dipole (or Raman emitter)–SPP coupling', and the second is 'Point dipole–image dipole' coupling. Now one can wonder how each coupling have an effect on formation of SERS image plane. Especially, if the first coupling takes part in major contribution on SERS image formation, Raman emission process can bring large distortion of intensity distribution in SERS images due to local

density of state (LDOS) along NW−axis.[38] [39]

To evaluate each contribution in generating SERS images, far−field imaging simulation based on FDTD method was adopted. In figure 24, schematic illustration of the model is depicted. On object plane (or sample plane), we can set positions of an AgNW dimer and a point dipole emitter which is approximation of single emissive Raman probe with specified amplitude. Then, plane waves will radiate from object plane to far−field region as we run a simulation. These plane waves (or rays) have various radiation angle and orientation. Using far−field projection based on Fourier transform, we can filter out these rays which have larger angle than the collection solid angle defined by numerical aperture (NA) of objective lens (NA = 1.4 for experimental setup). Then, using inverse Fourier transform, we can obtain image plane which is made of collected rays only.

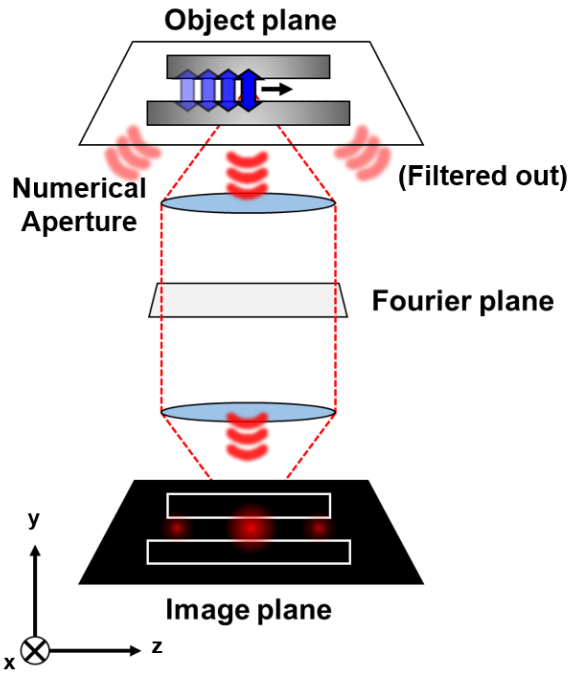

Figure 24. Simulation model for far-field imaging. Far-field images were simulated by projection of the calculated near-field intensity distribution recorded 10 nm below the structure in to the glass half-space taking the numerical aperture (NA) of the collection objective into account. All simulation results are for frequency of Raman shifted radiation of BPT.

By locating molecule (or point dipole emitter) in specific sites of AgNW dimer model based on AFM topography of figure 14 and observing changes of intensity and position of the image, we can infer the relation between molecule-NW coupling and SERS image formation.

Firstly, we need to check if the simulation model really works. If simulation model works well, overall shape and intensity of SERS image will be dramatically distorted as we pick out the radiating dipole from gap of AgNW dimer, or change the polarization of the dipole. (see figure 25) Comparing images (j) to (d) in figure 25, the far-field image of single dipole emitter located on top shows us

spread of light along NW−axis, which looks like leakage microscopy image of nanowires. When dipole source is located at top of nanowires, mode 4 in figure 20 is effectively excited so that SPP is leaked to glass substrate. Thus, it is reasonable that we can rely on this model to simulate the effect of molecular position on far−field image.

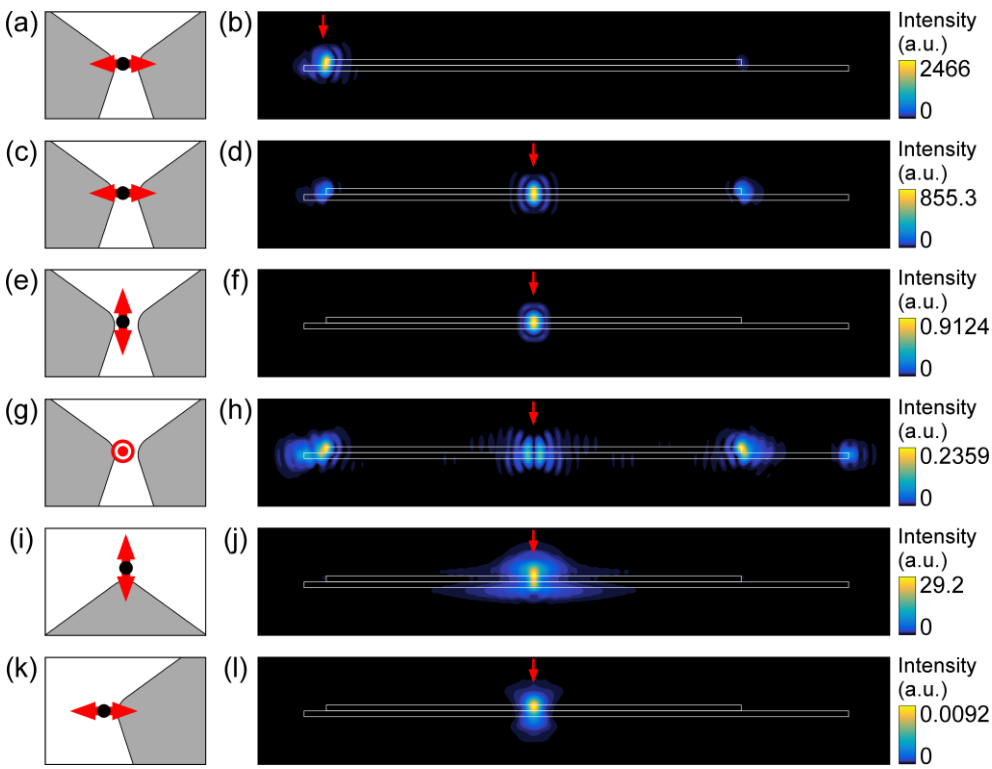

Figure 25. Simulated far−field images of a dipole emitter which is located at specific positions of AgNW dimer which is modeled on AFM topography in figure 12. **(a, c, e, g, i, and k)** cross−sectional view of dipole emitter (black dot combined with red arrow) and AgNW. **(b, d, f, h, j, and l)** Far−field images of a dipole emitter which is located at end or midpoint of AgNW dimer (marked by red arrow).

Now we can move dipole emitter inside the gap, along point by point on NW-axis. If the overall intensity is modulated dramatically like LDOS distribution of gap modes as we move dipole emitter, we should conclude that point dipole-SPP coupling mostly contribute to generation of far-field image, likely to SERS of nanoparticle dimer. If not, dipole-image dipole coupling will be the origin of enhancement in Raman emission process.

In figure 26 (a), the object plane of the simulation model is illustrated. As the dipole which has wavelength of 704 nm in vacuum (similar to Raman peak of 1611 cm^{-1} shifted from 632.8 nm) moves along NW-axis, near-field SPP intensity fluctuates dramatically. The intensity of SPP with periodicity of ~160 nm, which means that the SPP mostly consist of mode 1, is fluctuating dramatically as dipole emitter moves along NW-axis by 75 nm (almost half of the periodicity of SPP). Also, the intensity of SPP scattering at distal end of AgNW dimer is fluctuating with the same tendency. Thus, it is convincible that LDOS of mode 1 in the gap of silver nanowire dimer is successfully applied.

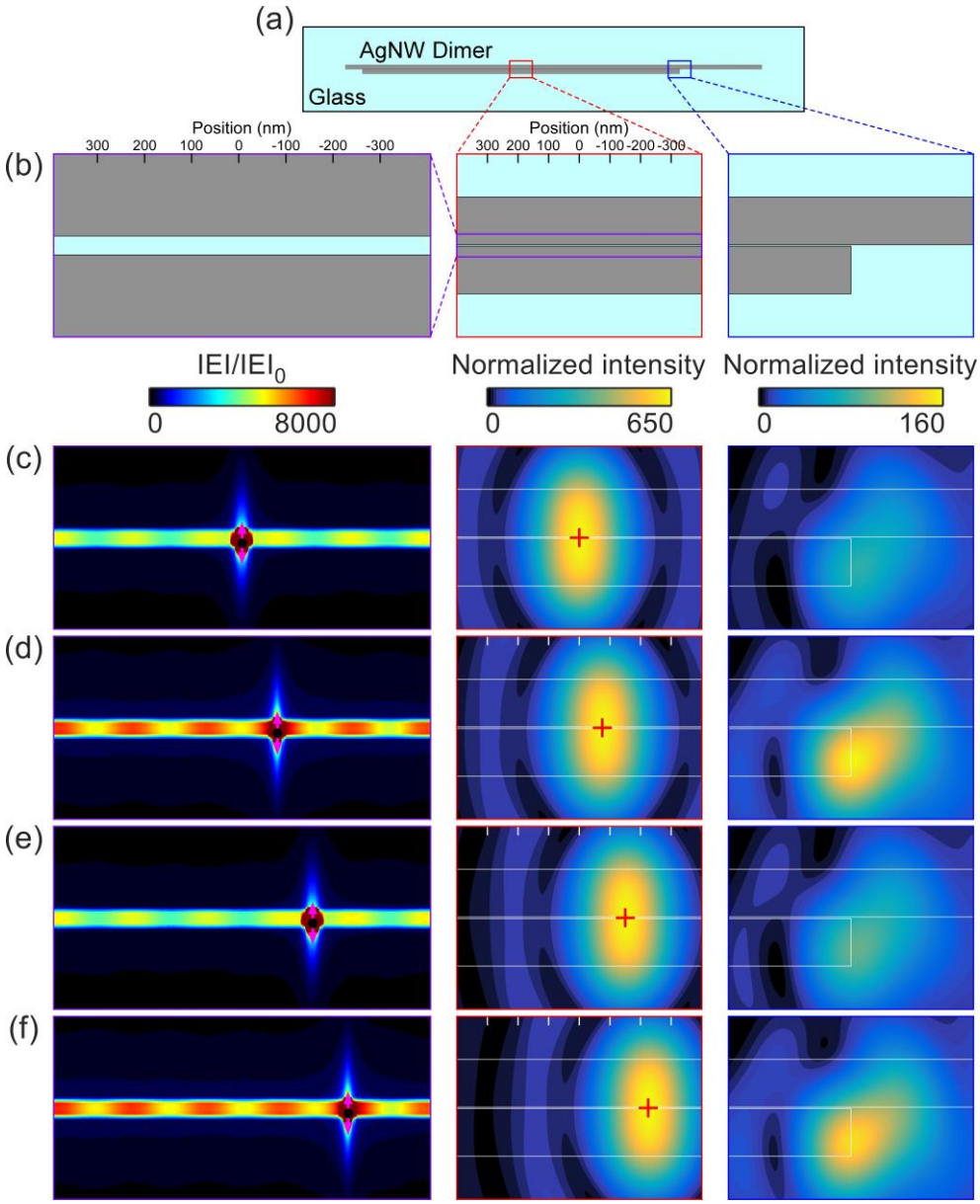

Figure 26. Results of Far-field imaging simulation for a dipole emitter of 704 nm wavelength. **(a)** Schematic illustration for the object plane. The structure of AgNW is modeled on the AFM topography in figure 14. **(b)** Magnified illustration for gap, midsection, and terminus of AgNW dimer. (from left to right) **(c-f)** Near-field distribution at gap around the dipole emitter, far-field image at position of the dipole emitter, and far-field image of SPP scattering at the terminus of AgNW dimer.

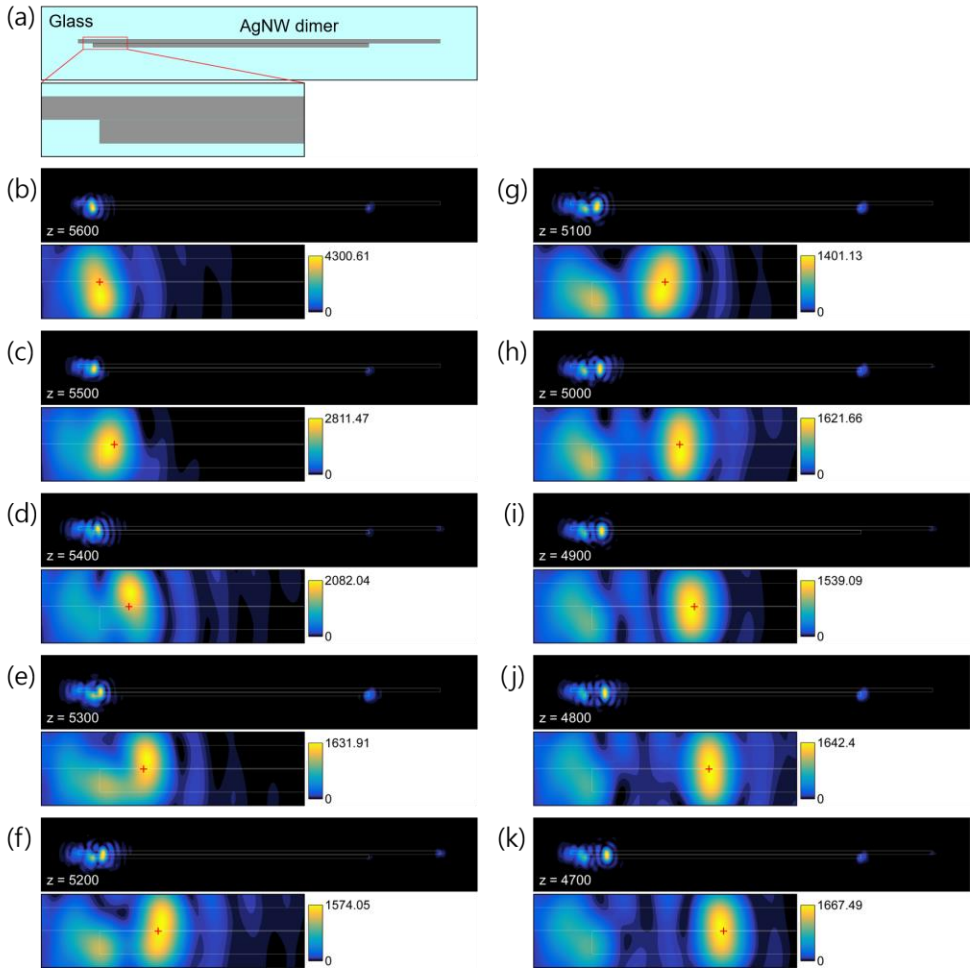

Figure 27. Simulated far-field image of single emitter at the gap of AgNW dimer. **(a)** Illustration for the object plane which has the same structure in figure 24. **(b-k)** Far-field image of single emitter which is in the gap near the terminus of AgNW dimer.

However, the intensity of far-field image at dipole emitter's position is maintained independently on local position of the dipole emitter. For exception, Raman emission enhancement become larger when molecule is in the gap near the terminus of the dimer. However, this effect diminishes as the position of molecule is at several hundred-nanometers away from the terminus. (see figure 27) Therefore, we can conclude that localized interaction, dipole emitter-image dipole coupling for example, dominates Raman emission enhancement at emitter's position. This will become obvious if the tendency of far-field intensity is maintained for another wavelength of Raman emitter. In figure 28, simulation results for another wavelength (680 nm for 1089 cm^{-1} and 689 nm for 1291.7 cm^{-1}) are shown.

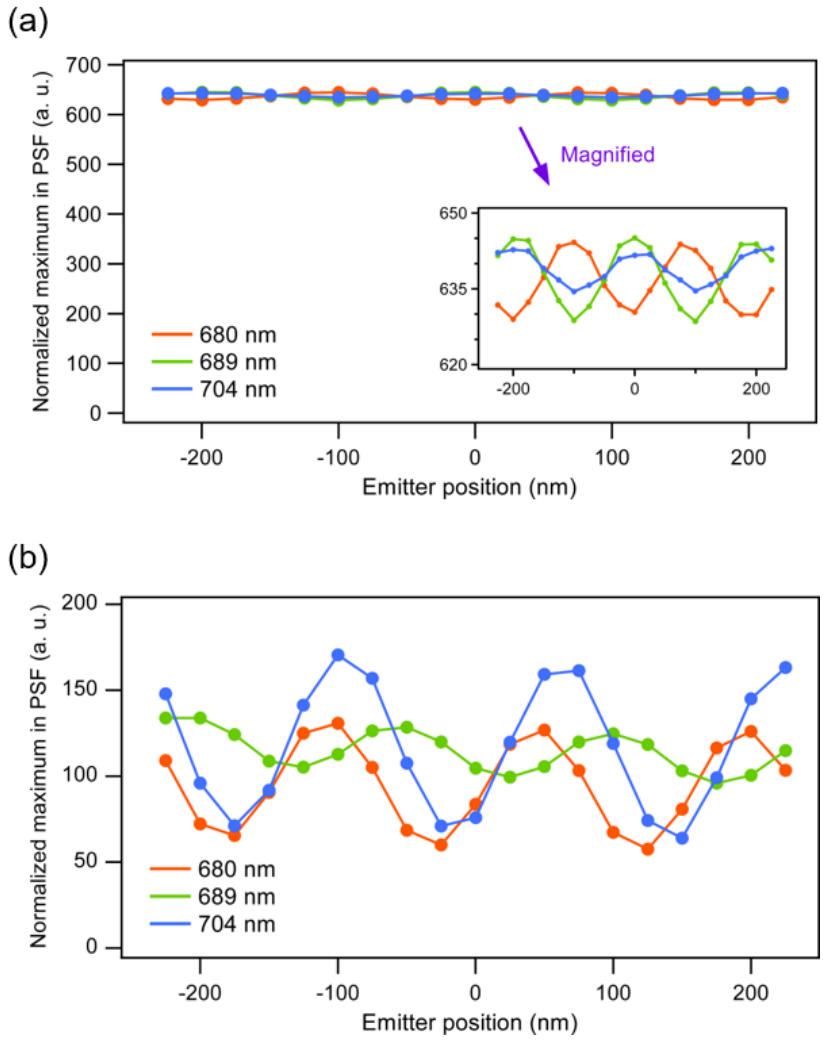

Figure 28. (a) Normalized maximum intensity in point spread function (PSF) of far-field image of the emitter related to the emitter's position. (b) Normalized maximum intensity in PSF of SPP scattering image at the distal end of AgNW dimer.

3.4. Conclusions and Outlook

In summary, by directly measuring image plane composed of SERS emission, we have experimentally proven that wide-field SERS microscopy can be used for characterization of SPP properties in narrow-gap waveguide. The oscillating intensity pattern in SERS image is originated from near-field distribution made of plasmon beating effect between two distinct gap modes.

Also, we have shown that far-field imaging simulation model can be used to determine how the coupling between emissive molecule and gap plasmon waveguide. For AgNW dimer, the radiating point dipole is enhanced by localized coupling which is almost independent on emitter's location. Thus, we have theoretically verified that Raman probes can be a tool for visualizing local field intensity distribution along one-dimensional gap plasmon waveguide.

The experimental method and the simulation model we have shown will help to expect and understand the distinct properties of gap plasmon waveguides and emitter-waveguide coupled systems which is needed for nanophotonic devices.

References

1. Ditlabcher, H., Hohenau, A., Wagner, D., Kreibig, U., Roger, M., Hofer, F., Aussenegg, F.R., & Krenn, J.R. Silver nanowires as surface plasmon resonators. *Phys. Rev. Lett.* 95, 257403-257406 (2005)

2. Imura, K. Kim, Y.C., Kim, S., Jeong, D.H., & Okamoto, H. Two-photon imaging of localized optical fields in the vicinity of silver nanowires using a scanning near-field optical microscope. *Phys. Chem. Chem. Phys.* 11, 5876-5881 (2009)

3. Venugopalan, P., Zhang, Q., Li, X., & Gu, M. Propagating plasmonic modes in silver nanowire waveguide on a glass substrate with a scanning near-field optical microscope. *Opt. Express* 21 (13), 15247-15252 (2013)

4. Kang, T., Kim, H., Lee, J. M., Lee, H., Choi, YS., Kang, G., Seo, MK., Chung, B.H., Jung, Y., & Kim, B. Ultra-specific zentomole microRNA detection by plasmonic nanowire interstice sensor with bi-temperature hybridization. *Small* 10 (20), 4200-4206 (2014)

5. Fujita, Y., Walke, P., Feyter, S.D., & Uji-i, H. Remote excitation-tip-enhanced Raman scattering microscopy using silver nanowire. *Jpn. J. Appl. Phys.* 55, 08NB03-1 (2016)

6. Fang, Y., Wei, H., Hao, F., Nordlander, P., & Xu, H. Remote-excitation surface-enhanced Raman scattering using propagating Ag nanowire plasmons. *Nano Lett.* 9 (5), 2049-2053 (2009)

7. Hutchson, J.A., Centeno, S.P., Odaka, H., Fukumura, H, Hofkens, J., & Uji-i, H. Subdiffraction limited, remote excitation of surface enhanced Raman scattering. *Nano Lett.* 9 (3), 995-1001 (2009)

8. Li, Y., Kang, M, Shi, J., Wu, K., Zhang, S., & Xu, H. Transversely divergent second harmonic generation by surface plasmon polaritons on single metallic nanowires. *Nano Lett.* 17 (12), 7803-7808 (2017)

9. Wei, H., Li, Z., Tian, X., Wang, Z., Cong, F., Liu, N., Zhang, S., Nordlander, P., Halas, N.J., & Xu, H. Quantum dot-based local field imaging reveals plasmon-based interferometric logic in silver nanowire networks. *Nano Lett.*, 11 (2), 471-475 (2011)

10. Zhang, S., Wei, H., Bao, K., Hakanson, U., Halas, N.J., Nordlander, P., & Xu, H. Chiral surface plasmon polaritons on metallic nanowires. *Phys. Rev. Lett.* 107, 096801-096805 (2011)

11. Li, Q., Wei, H., & Xu, H., Resolving single plasmons generated by multiquantum-emitters on a silver nanowire. *Nano Lett.* 14 (6), 3358-3363 (2014)

12. Juan, M.L., Righini, M., & Quidant R. Plasmon nano-optical tweezers. *Nat. Photon.* 5, 349-356 (2011)

13. Song, M., Bouhelier, A., Bramant, P., Sharma, J., Dujardin, E., Zhang, D., & Colas-des-Francs, G. Imaging symmetry-selected corner plasmon modes in penta-twinned crystalline Ag nanowires. *ACS Nano* 5 (7), 5874-5880 (2011)

14. Sun, S., Chen, HT., Zheng, WJ., & Guo, GY. Dispersion relation, propagation length and more conversion of surface plasmon polaritons in silver double-nanowire systems. *Opt. Express* 21 (12), 14591-14605 (2013)

15. Manjavacas, A., & Garcia de Abajo, F.J. Robust plasmon waveguides in strongly interacting nanowire arrays. *Nano Lett.* 9 (4), 1285-1289 (2009)

16. Bora, M., Fasenfest, B.J., Behymer, E.M., Chang, A.SP., Nguyen, H.T, Britten, J.A., Larson, C.C, Chan, J.W., Miles, R.R., & Bond, T.C. Plasmon resonant cavities in vertical nanowire arrays. *Nano Lett.* 10 (8), 2832-2837 (2010)

17. Johnson, P.B., & Christy, R.W. Optical constants of the noble metals. *Phys. Rev. B.* 6, 4370-4379 (1972)

18. Wei, H., Zhang, S., Tian, X., & Xu, H. Highly tunable propagating surface plasmons on supported silver nanowires. *Proc. Nat. Acad. Sci. USA.* 110 (12), 4494-4499 (2013)

19. Su, L., Lu, G., Kenens, B., Rocha, S., Fron, E., Yuan, H., Chen, C., Van Dorpe, P., Roeffaers, M.B.J, Hofkens, J., Hutchson, J.A. & Uji-i, H. Visualization of molecular fluorescence point spread functions via remote excitation switching fluorescence microscopy. *Nat. Comm.* 6, 6287-6295 (2015)

20. Solis, D., Chang, WS., Khanal, B.P., Bao, K., Nordlander, P., Zubarev, E.R., & Link, S. Bleach-imaged plasmon propagation (BlIPP) in single gold nanowires. *Nano Lett.* 10 (9), 3482-3485 (2010)

21. Stoermer, R.L, & Keating, C.D. Distance-dependent emission from dye-labeled oligonucleotides on striped Au/Ag nanowires: effect of secondary structure and hybridization efficiency. *J. Am. Chem. Soc.* 128 (40), 13243-13254 (2006)

22. Kim, DS., Heo, J., Ahn, SH., Han, S.W., Yun, W.S., & Kim, Z.H. Real-space mapping of the strongly coupled plasmon of nanoparticle dimers. *Nano Lett.* 9 (10), 3619-3625 (2009)
23. Raman, C.V., & Krishnan, K.S. A new type of secondary radiation. *Nature* 121, 501-502 (1928)

24. Krishnan, R.S., & Shankar, R.K. Raman effect: history of the discovery. *J. Raman Spectrosc.* 10 (1), 1-8 (1981)

25. Fleishmann, M., Hendra, P.J., & Mcquillan, A.J. Raman spectra of pyridine adsorbed at a silver electrode. *Chem. Phys. Lett.* 26 (2), 163-166 (1974)

26. Jeanmaire, D.L., & Van Duyne, R.P. Surface Raman spectroelectrochemistry: part I. heterocyclic, aromatic, and aliphatic amines adsorbed on the anodized silver electrode. *J. Electroanal. Chem. Interfacial Electrochem.* 84 (1), 1-20 (1977)

27. Albrecht, M.G., & Creighton J.A. Anomalously intense Raman spectra of pyridine at a silver electrode. *J. Am. Chem. Soc.* 99 (15), 5215-5217 (1977)

28. Li, W., Camargo, P.H.C., Lu, X., & Xia, Y. Dimers of silver nanoparticles: facile synthesis and their use as hot spots for surface-enhanced Raman scattering. *Nano Lett.* 9 (1), 485-490

(2009)

29. Weber, M.L., & Willets, K.A. Correlated super-resolution optical and structural studies of surface-enhanced Raman scattering hot spots in silver colloid aggregates. *J. Phys. Chem. Lett.* 2 (14), 1766-1770 (2011)

30. Lombardi, A., Demetriadou, A., Weller, L., Andrae, P., Benz, F., Chikkaraddy, R., Aizpurua, J., & Baumberg, J.J. Anomalous spectral shift of near- and far-field plasmonic resonances in nanogaps. *ACS Photon.* 3 (3), 471-477 (2016)

31. Ding, SY., You, EM., Tian, ZQ., & Moskovits, M. Electromagnetic theories of surface-enhanced Raman spectroscopy. *Chem. Soc. Rev.* 46 (13), 4042-4076 (2017)

32. Coskun, S., Aksoy, B., & Unalan, H. E. Polyol synthesis of silver nanowires: an extensive parametric study. *Cryst. Growth Des.* 11 (11), 4963-4969 (2011)

33. Sun, Y., Ren, Y., Liu, Y., Wen, J., Okasinski, J.S. & Miller, D.J. Ambient-stable tetragonal phase in silver nanostructures. *Nat. Commun.* 3, 971- 976(2012)

34. Liang, Z., & Graham, K.R. Surface modification of silver nanowires for morphology and processing control in composite transparaent electrodes. *ACS Appl. Mater. Interfaces* 7 (39), 21652-21656 (2015)

35. Frisch, M.J., Trucks, G.W., Schlegel, H.B., Scuseria, G.E., Robb, M.A., Cheeseman, J.R., Scalmani, G., Barone, V., Mennucci, B., Petersson, G. A., Nakatsuji, H., Caricato, M., Li, X., Hratchian, H.P., Izmaylov, A.F., Bloino, J., Zheng, G., Sonnenberg, J.L., Hada, M., Ehara, M., Toyota, K., Fukuda, R., Hasegawa, J., Ishida, M., Nakajima, T., Honda, Y., Kitao, O., Nakai, H., Vreven, T., Montgomery Jr., J.A., Peralta, J.E., Ogliaro, F., Bearpark, M.J., Heyd, J., Brothers, E.N., Kudin, K.N., Staroverov, V.N., Kobayashi, R., Normand, J., Raghavachari, K., Rendell, A. P., Burant, J. C., Iyengar, S. S., Tomasi, J., Cossi, M., Rega, N., Millam, N. J., Klene, M., Knox, J. E., Cross, J. B., Bakken, V., Adamo, C., Jaramillo, J., Gomperts, R., Stratmann, R. E., Yazyev, O., Austin, A. J., Cammi, R., Pomelli, C., Ochterski, J.W., Martin,

R.L., Morokuma, K., Zakrzewski, V.G., Voth, G.A., Salvador, P., Dannenberg, J.J., Dapprich, S., Daniels, A.D., Farkas, Ö., Foresman, J.B., Ortiz, J.V., Cioslowski, J., & Fox, D.J. *Gaussian 09. Rev. B01 ed.*, Gaussian Inc., Wallingford, CT (2009)

36. Jia, Z., Wei, H., Pan, D., & Xu, H. Direction-resolved radiation from polarization-controlled surface plasmon modes on silver nanowire antennas. *Nanoscale* 8 (48), 20118-20124 (2016)
37. Itoh, T., Yamamoto, Y.S., Kitahama, Y., & Balachandran, *J. Phys. Rev. B* 95, 115441-115448 (2017)

38. Ropp, C., Cummins, Z., Nah, S., Fourkas, J.T., Shapiro, B., & Waks, E. Nanoscale probing of image-dipole interactions in a metallic nanostructure. *Nat. Commun.* 6, 6558-6565 (2015)

39. Ropp, C., Cummins, Z., Nah, S., Fourkas, J.T., Shapiro, B., & Waks, E. Nanoscale imaging and spontaneous emission control with a single nano-positioned quantum dot. *Nat. Commun.* 4, 1447-1454 (2013)

Abstract (in Korean)

표면증강라만산란을 응용한 은 나노선 이합체의 플라즈모닉 핫스팟에 대한 직접적 가시화

표면 플라즈몬 폴라리톤 (SPP)에 대한 시각적 분석은, 회절한계 이하의 광집적소자의 기본 구성요소가 되는 플라즈몬 도파관 (Plasmon waveguide)의 특성을 파악하는데 있어 필수적인 과정이다. 형광이 갖는 장점을 이용한 형광기반의 현미경법은 통상적으로 측정과정에서 나타나는 깜빡임, 형광성의 소실, 금속 표면에 의한 형광의 소광과 같은 문제로 인해 좁은 간극을 갖는 플라즈모닉 구조체에는 적용하기 힘들다. 마찬가지로, 팁 기반의 현미경법의 경우 팁의 사용으로 인해 나타나는 문제로 인해 좁은 간극의 플라즈모닉 구조체에는 적용되기 힘들다. 그러나, 표면증강라만산란 (SERS)를 사용한 현미경법은 상대적으로 그러한 문제에서 자유롭기 때문에 간극을 갖는 플라즈몬 도파관에서 나타나는 국지적인 전기장을 시각화 할 수 있는 대안이 된다.

이 연구에서는, 화학적으로 합성된 은 나노선 이합체에서 나타나는 SERS 이미지 상의 세기 분포에 대해 은 나노선의 장축을 따라 공간적인 변형이 발생하는 현상을 다루었다. 이에 대한 해석으로서, 실험적으로 관찰한 SERS 신호 세기의 분포양상은 두 개의 서로 다른 SPP 고유모드 간에 발생하는 비팅 현상 (Mode beating)에 의해 나타나는 것으로 설명할 수 있다. 또한 더 나아가서, 일반적으로 SERS 현상을 관찰하는데 사용하는 나노입자 이합체의 경우와 달리, 나노선 이합체에서의 SERS 신호 방사현상이 국지적인 전기장의 분포와 세기를 직접적으로 반영할 수 있음을 이론적으로 검토하였다.